

Point Spread Function Estimation With Blind Deconvolution in Structured Illumination Microscopy

X. Liu Student

Master of Science Thesis

Point Spread Function Estimation With Blind Deconvolution in Structured Illumination Microscopy

MASTER OF SCIENCE THESIS

For the degree of Master of Science in Embedded Systems at Delft
University of Technology

X. Liu Student

June 22, 2020

Faculty of Electrical Engineering, Mathematics and Computer Science (EEMCS) · Delft
University of Technology



Copyright © Delft Center for Systems and Control (DCSC)
All rights reserved.



Abstract

Structured illumination microscopy (SIM) is a kind of wide-field super resolution imaging technique which achieves the resolution improvement by exploiting the interference patterns to obtain the information out of the observable region in Fourier space[1]. The resolution improvement in SIM is done by analyzing the obtained image and restored the observed sample with software. This process is sensitive to the measured PSF, as the PSF is the main factor to do the image deblurring and parameters estimation.

Frequently, the PSF of a SIM system is obtained by fitting the recorded beads image with the Gaussian function[2]. However, the Gaussian fitting can not retrieve the aberration and noise in the PSF.

The blind image deconvolution method is a family of algorithms which can be used to restored the object and corresponding PSF from the degraded images. The novel Tangential Iterative Projections (TIP) algorithm is a kind of blind image deconvolution algorithm proposed by Wilding *et al.*. This algorithm is simple, fast and robust to the noise condition. It is proved that TIP can be implemented on both the multi-frame deconvolution scenario and single-frame scenario[3, 4].

The aim of this thesis is to verify whether TIP algorithm can retrieve a PSF, which can be used to do the SIM image reconstruction, from the SIM data. For this purpose, a simulated SIM optical system is built in Matlab to generate the SIM images, and both the single-frame TIP and multi-frame TIP frameworks are used to do the PSF retrieval. In addition, a new constraint for the PSF which is generated based on the diffraction limit of the optical system is implemented. In order to reduce the execution time and avoid the overfitting of the algorithm, a stop criterion is introduced.

The result shows both the multi-frame TIP and single-frame TIP can be used to retrieve an effective PSF from the SIM data, and the single-frame TIP is more applicable and accuracy compared with the multi-frame TIP.

Table of Contents

Acknowledgements	xi
1 Introduction	1
2 Optical Imaging and Super Resolution Technique	3
2-1 Image Formation in an Optical Imaging System	3
2-1-1 Basic concept of Optics	3
2-1-2 The Point Spread Function	4
2-2 Super Resolution Technique	6
2-3 The principle of SIM	11
2-3-1 Image Formation and Reconstruction in SIM	12
2-3-2 Parameter estimation	14
2-4 Summary	16
3 TIP algorithm	19
3-1 Multi-frame TIP	20
3-2 Single-frame TIP	21
3-3 Summary	23
4 PSF Estimation with TIP Algorithm in SIM	25
4-1 TIP with raw images	25
4-2 TIP with wide-field image	27
4-3 Constraints	28
4-4 Stop Criterion	31
4-5 Summary	34

5	Result	35
5-1	SIM image generation	35
5-2	The impact of SNR on PSF estimation	36
5-3	The impact of the aberration strength of the PSF on the PSF estimation	38
5-4	Compare the SF-TIP with the Gaussian curve fitting	39
5-5	Summary	43
6	Conclusion and Future work	45
6-1	Conclusion	45
6-2	Future work	46
A	Simulation of the Structured Illumination Microscopy	47
A-1	SIM Image generation	47
A-1-1	Object preparation	47
A-1-2	PSF generation	48
A-1-3	Illumination pattern	49
A-1-4	Image Acquisition	51
A-2	Image reconstruction	51
A-2-1	Parameters estimation	52
A-2-2	Reconstruction with Wiener filter	52
B	User-defined parameters	55
C	Measure the resolution of the image	57
C-1	Measure the quality of the restored image	57

List of Figures

2-1	The first 15 Zernike Polynomials in Cartesian coordinates.[5]	5
2-2	Left: The Point spread function of a system. Right: The cross-section plot of the PSF. ([6])	7
2-3	Optical scheme in 4Pi microscope [7]	7
2-4	Optical scheme in I ⁵ M microscope [7]	7
2-5	The axial slice in 4Pi and I ⁵ M. (a) shows the typical section of the 3D image recorded by the 2PE PI of type C. The dashed line in the inset of figure (a) illustrate the position of xz-slice in the xy-overview. Figure (c) shows the deconvolution result of the figure (a). Figure (c) and (d) shows the recorded image and the deconvoluted image in I ⁵ M. The inset of the figure (c) shows the position of xz-slice in the xy-overview. [7]	8
2-6	Optical scheme in STED [8]	9
2-7	Fluorescent nanoparticles imaged by confocal microscopy (left) and STED microscopy (right) [9].	9
2-8	The process of super resolution imaging in SMLM [10]	10
2-9	The image of confocal microscopy (left) and photoactivated localization microscopy (right) [11]	10
2-10	The principle of resolution improvement in structured illumination microscopy.(a) The support region of optical transfer function which is the observable region of the conventional microscope in Fourier domain. The three dots in (b) describes three information component. After getting the shifting-phase, these superimposed components can be shift back to their original position resulting in an expanded observable region (c). Rotate the illumination in three orientations to expand the resolution isotropically. [12]	11
2-11	The image of the conventional wide-field microscope (a) and the SIM (b). [12]	12
2-12	The cross-section plot of the distance transform result (left) and the Apodization filter (right).	14

2-13	Illustration of the subpixel detection. (a) and (b) are raw image and its Fourier spectrum respectively. The wave vector is shown in (b). (c) shows the peak location mismatch, the green and red cross in (c) indicate the actual location and the location estimated with the original image. (d) shows the result of the proposed subpixel detection method.	16
2-14	The overlapping spectrum. The blue arrow indicates the wave vector \vec{p} , by which the information component \tilde{C}'_1 is shifted back to its correct position. As shown, there is an overlap region. The two spectrum in this overlap region is differ by a complex number. When $a_0 = 1$, the absolute value of this complex number is the modulation depth (See Eq.2-26).	17
3-1	The diagram of the multi-frame TIP. This framework contains 4 steps. \mathcal{P}_1 and \mathcal{P}_3 are linear deconvolution. \mathcal{P}_2 and \mathcal{P}_4 are the projection to the feasible set \mathcal{O} and \mathcal{H} respectively [3].	21
3-2	The illustration about how to split the single-frame image into several patches [4].	23
3-3	The diagram of the single framework. This framework contains 5 steps. The first one is the image preparation while the other four steps are the projection steps. \mathcal{P}_1 and \mathcal{P}_4 are linear deconvolution. \mathcal{P}_2 and \mathcal{P}_3 are the projection to the feasible set \mathcal{H} and \mathcal{O} respectively [4]	24
4-1	The flowchart of the MF-TIP algorithm in SIM. Four projection steps are shown in flowchart and the corresponding operations are shown by the lines between the boxes. \mathcal{P}_1 is the multi-frame linear deconvolution, \mathcal{P}_2 is the projection to the feasible set of the PSFs, \mathcal{P}_3 is the linear deconvolution for each frame, \mathcal{P}_4 is the projection to the feasible set of the object. ∇R is the first derivation of the resolution.	26
4-2	The flowchart of the SF-TIP algorithm in SIM . The image is first split into several patches to create the images for the different objects. Then the multi-frame linear deconvolution is done in the \mathcal{P}_1 . In \mathcal{P}_2 , the PSF estimate is projected to its support region to get the estimated PSF. Then the linear deconvolution is done in \mathcal{P}_3 . Finally, the projection process for the estimate object is done in \mathcal{P}_4 . ∇R is the first derivation of the resolution.	27
4-3	The binary mask generated based on the diffraction limit. The radius of this mask is $d = \frac{\lambda}{2NA}$	29
4-4	The mean PSNR of the PSF for 160 different image-PSF pairs deconvolved using the four TIP frameworks. The label of each curve are shown at the bottom right corner in the figure. The errorbar shows the standard derivation.	30
4-5	The relationship between the mean resolution and the number of iteration of the TIP algorithm.	30
4-6	The distribution of the minimum resolution of the images restored from the 160 image-PSF pairs with different RMS in 100 iterations.	31
4-7	The deconvolution result of the SIM data for four TIP frameworks and the first derivative $\nabla Resolution$ of these deconvolution result respectively. The dash line shows the corresponding iteration for each TIP framework when -2 is used as threshold.	32
4-8	The deconvolution result of the SIM data for four TIP frameworks and the first derivative $\nabla Resolution$ of these deconvolution result respectively. The dash line shows the corresponding iteration for each TIP framework when -1 is used as threshold.	32
4-9	The deconvolution result of the SIM data for four TIP frameworks and the first derivative $\nabla Resolution$ of these deconvolution result respectively. The dash line shows the corresponding iteration for each TIP framework when -0.2 is used as threshold.	33

4-10	The comparison of the distribution of the minimum resolution of the SF-TIP and the resolution of the image restored with the PSF estimate at the stop criterion.	33
4-11	The comparison of the distribution of the minimum resolution of the MF-TIP and the resolution of the image restored with the PSF estimate at the stop criterion.	34
5-1	The object used in simulation	36
5-2	The illuminations in three orientations	36
5-3	The example of the PSF and its corresponding OTF	37
5-4	The example of simulated raw images in three orientations	37
5-5	From left to right are the object, the wide-field image and the reconstructed image.	37
5-6	The PSNR curve for the PSF retrieve from the widefield image with different SNR using SF-TIP.	38
5-7	The mean and standard deviation of the error of phases estimation. With the increase of the aberration strength, both the mean and the std of the phase estimation error increase.	39
5-8	The distribution of the resolution of the wide-field images and their corresponding restored images. The resolution of the restored image shows a more than 300nm increase. To make the figure more readable, the outliers for the boxplot which is larger than 800nm are removed.	40
5-9	The mean factor of the resolution improvement of 160 image-PSF pairs with 8 aberration strength. Errorbar shows the standard derivation of the factor.	40
5-10	The comparison of the mean and standard deviation of the phases estimation error for three different kinds of PSF. In the low aberration strength condition, the performance of these three kinds of PSF are similar. With the increase of the aberration strength, the performance of both the Gaussian PSF and the TIP PSF become worse.	41
5-11	The distribution of the resolution of the restored images. The red boxes represent the data for the images restored with the actual PSF, the green boxes are the data for the image restored with the TIP PSF, and the blue boxes are the data for the images restored with the Gaussian PSF. With the increase of the intensity of the aberration, the performance of Gaussian PSF is decreased, and this kind of PSF is not suitable for image reconstruction.	42
5-12	The mean factor of the resolution improvement. With the increase of the aberration strength, the stability of the performance of the TIP algorithm decreases. But the mean factor of the TIP PSF is closer to the mean factor for the Actual PSF compared with the factor of the Gaussian PSF	42
5-13	The example of the actual PSF and the estimated PSFs. Compared with the Gaussian fitting method, the TIP algorithm performance better in the PSF estimation, since the TIP algorithm is better at retrieving the aberration in the PSF.	43
A-1	Prepared object for which $N_{ph} = 1e16$ and $N_{bg} = 20$. The size of this object is $512*512$	48
A-2	The simulated PSF	49
A-3	The example of the OTF of which the out-of-band noise is removed.	50
A-4	The illuminations in three orientations	50
A-5	The example of the SIM raw image.	51
A-6	The wide-field image of the SIM which is the sum of 9 SIM raw images.	52
A-7	The shifted Fourier components and the shifted OTF in one orientation.	53

A-8	The possible apodization filters. The LukoszBound is more benign than the tranglex filter for the optimizing the contrast.	54
A-9	The comparison of the wide-field image and the restored image. The maximum radius of circle in the wide-field image (left) is larger than the maximum radius of the circle in the restored image (right).	54
C-1	The restored Siemens star image.	57
C-2	The two sub-images of the Figure C-1 split using binomial random distribution. .	58
C-3	The example of the FRC curve and the 1/7 threshold to get the resolution. The real space distance of the x axis value of th cross is the resolution of the image.	58

List of Tables

3-1	The description of each step of the TIP algorithm [3]	22
3-2	The description of each step of single-frame TIP algorithm	24
4-1	The probability of the error between the minimum resolution and the resolution of the image restored with the PSF estimated at the stop criterion.	34
5-1	The success rate of the image reconstruction using the PSF estimated with different algorithms.	44

Acknowledgements

I would like to thank my supervisors Dr. Carlas Smith and Dr. Oleg Soloviev for their excellent guidance. Writing this thesis is a long process, thanks for keeping me positive and encouraging me not to give up. Thanks for all the comments and remarks you have given to me.

I would like to thank all Numerics for Control & Identification members for their patience, help and knowledge sharing. No matter how simple and stupid my question is, they will answer patiently. It is a pleasure to work with them.

Thanks for all the friends I have met here who make the study in Delft an unforgettable and amazing experience. Without your company, the life in Netherlands will be less colorful.

Finally, I would like to thanks my parents. They always give me unconditional support and love.

Delft, University of Technology
June 22, 2020

X. Liu Student

“Nothing will work unless you do.”

— *Maya Angelou*

Chapter 1

Introduction

Over the past decades, fluorescence microscopy has become an essential tool in the observation of the biological structures. The resolution of the conventional fluorescent microscopy is restricted by the diffraction limit, about 200 300 nm in the lateral direction and 500 700 nm in the axial direction [13]. Some biological structures are smaller than this limit and are too small to be observed in detail. To reveal the details of these small cellular structures, the super resolution microscopy is developed. The most common used super resolution microscopy are Stimulated emission depletion (STED) microscopy, the Single-molecule localization microscopy (SMLM) and the structured illumination microscopy (SIM). Compared to the other super resolution techniques, SIM does not have special requirement of the fluorophores, and can be used to image both the fixed and living object [1, 14]. Therefore SIM is widely used in the biomedical science.

The frequently used image reconstruction algorithms in SIM are Richardson-Lucy algorithm and Wiener filter. Both of these methods require the known point spread function (PSF). This PSF is always obtained by the experimental measurement. This method is achieved by recording images of the small beads. These obtained images are averaged and then used to calculate the PSF. This experimental PSF includes all the physical deviations of the imaging system, however, the beads are not the real point source, which will enlarge the PSF and cause problem in image restoration.

Considered that the experimental PSF will reduce the quality of the restored image, is it possible to use other methods to get the PSF and the object? Then the problem becomes a blind image deconvolution problem.

Filip Sroubek and Peyman Milanfar presented a noise robust multichannel blind deconvolution method based on the alternative minimization method [15]. In this method, for each iteration, the image deconvolution is split into o-step and h-step which are used to estimated the object and the PSF respectively.

Wilding *et al.*[3] present the tangential iterative projection algorithm to solve both the multi-frame and single-frame blind image deconvolution problem. For each iteration, the algorithm

contains four steps, two linear deconvolution steps and two projection steps which is used to reduce the error in the estimated PSF and object.

The objective of this thesis is to find a method to estimate the PSF of the SIM, of which the estimated PSF is accurate enough and can be used as a prior knowledge in the image restoration process. By comparing the characteristics of different blind image deconvolution algorithms, the TIP algorithm is the most applicable algorithm as it is noise robust, low computational complexity and can work on data at low signal-to-noise ratios. Then the research question can be narrowed down to:

Whether the TIP algorithm can retrieve the PSF, which can be used to do the SIM image reconstruction from SIM raw data?

The structure of the thesis is following. First, the principle of the optical imaging and the basic theory of the structured illumination microscopy are introduced in the Chapter 2. Then the method that can be used to obtain the PSF with a set of images are described in Chapter 3, followed by the introduction of how to implement the PSF estimation algorithm with SIM data in Chapter 4. The result of the SIM simulation and the limitation of the algorithm are shown in Chapter 5. Finally, the conclusions are drawn in Chapter 6.

Optical Imaging and Super Resolution Technique

In this chapter, the mathematical model for the image formation in an optical system and how the super resolution techniques break the diffraction limit are introduced.

2-1 Image Formation in an Optical Imaging System

Optical imaging systems are used in different types of application to achieve object observation and image acquisition. In geometric optics, the light is treated as a ray, which means the propagation distance of the light can be arbitrarily extended and the beam do not have width. However, some optical phenomena, like diffraction can not be explained by geometric optics. Thus, the physical optics is introduced. In physical optics, the light is considered as electromagnetic radiations which have the properties of wave [5]. The wave-nature of the light emitted by the point source will cause the degradation of the obtained image. The image captured by the imaging system is not a point again. In this section we follow the reasoning and use the formulas of the [5].

2-1-1 Basic concept of Optics

In physical optics, the light is considered to propagate as a wave. Based on the scalar wave theory, the light wave can be described as

$$u(\vec{r}, t) = a(\vec{r}) \cos(\omega t - \psi(\vec{r})) = a(\vec{r}) \operatorname{Re} e^{i(\omega t - \psi(\vec{r}))} = \operatorname{Re} a(\vec{r}) e^{-i\psi(\vec{r})} e^{i\omega t} = \operatorname{Re} A(\vec{r}) e^{i\omega t}, \quad (2-1)$$

in which t is the time, \vec{r} is the spatial coordinate, $a(\vec{r})$ represent the amplitude, $A(\vec{r})$ is the complex amplitude, ω denote the angular frequency of the light, and $\psi(\vec{r})$ describe the initial phase delay in the spatial coordinate.

A point source will emit light in all directions. As a result, the wavefront of this point source is spherical in shape and the expression of the wave light is

$$A(\vec{r}) = \frac{A_0(\vec{r})}{d} e^{-i\omega t} = \frac{A_0(\vec{r})}{d} e^{i\frac{2\pi c}{\lambda} \frac{d}{c}} = \frac{A_0(\vec{r})}{d} e^{-ikd}, \quad (2-2)$$

where $A_0(\vec{r})$ is the initial complex amplitude at 1m, d is the distance that the wave propagated, $k = \frac{2\pi}{\lambda}$ denotes the wavenumber which is the spatial frequency of the wave. Assume that $A_0(\vec{r})$ is the complex amplitude at point $\vec{r}_0 = (x_0, y_0, z_0)$, then the expression of the spherical wave at $\vec{r} = (x, y, z)$ is given by

$$A(\vec{r}) = \frac{A_0(\vec{r})}{|\vec{r} - \vec{r}_0|} e^{-ik|\vec{r} - \vec{r}_0|} = \frac{a_0}{|\vec{r} - \vec{r}_0|} e^{-ik|\vec{r} - \vec{r}_0| - i\psi_0}, \quad (2-3)$$

where a_0 is the initial amplitude and ψ_0 is the initial phase.

In the imaging process, the light passes through the optical system and specimen, during which the aberration is introduced causing the distortion of the wavefront. Both the imperfect optical components and the misalignment of the imaging system can cause aberration in the wavefront. Besides, the external factors, such as the inhomogeneous medium and the thermal blooming, also lead to the aberration in the wavefront. The wavefront is a surface over which the optical wave has a constant phase. The phase aberrations are changes in the wavefront. Therefore, after introducing the phase aberration, the wavefront is not a ideal shape anymore.

Zernike Polynomials

The shape of the wavefront influences the performance of the optical system. The wavefront is changed by the phase aberrations, and the standard method to describe these aberrations is using some predefined functions. In optics, a weighted sum of Zernike Polynomials is used to described the wavefront aberrations:

$$w(x, y) = \sum_{m,n} a_n^m Z_n^{\pm m}(x, y), \quad (2-4)$$

where a_n^m is the weight for the Zernike Polynomial Z_n^m for which m and n are two non-negative integer that

$$m, n \in \mathbb{Z}_{\geq 0}, \quad n \geq m, \quad n - m \in 2\mathbb{Z}. \quad (2-5)$$

Noll introduced a modified notation of Zernike polynomials in [16] where the Zernike polynomials are numbered with single index. Figure 2-1 shows the first 15 Zernike polynomials in Cartesian coordinates and its corresponding PSF.

2-1-2 The Point Spread Function

The wavefront can be controlled by introducing extra phase delay with the optical components. This can be done by introducing the lens in the optical system. The positive lens can convert the plane wave into a spherical wave converging to a point at the focal plane.










Index	Noll's ordering	Name	Expression	Shape	PSF
$Z_0^0(x, y)$	1	piston	1		
$Z_1^1(x, y)$	2	tip	x		
$Z_1^{-1}(x, y)$	3	tilt	y		
$Z_2^0(x, y)$	4	defocus	$2x^2 + 2y^2 - 1$		
$Z_2^2(x, y)$	5	astigmatism	$x^2 - y^2$		
$Z_2^{-2}(x, y)$	6	astigmatism	$2xy$		
$Z_3^1(x, y)$	7	coma	$3x^3 + 3y^2x - 2x$		
$Z_3^{-1}(x, y)$	8	coma	$3y^3 + 3x^2y - 2y$		
$Z_3^3(x, y)$	9	trefoil	$x^3 - 3xy^2$		
$Z_3^{-3}(x, y)$	10	trefoil	$3x^2y - y^3$		
$Z_4^0(x, y)$	11	spherical	$6x^4 + 12y^2x^2 - 6x^2 + 6y^4 - 6y^2 + 1$		
$Z_4^2(x, y)$	12		$4x^4 - 3x^2 - 4y^4 + 3y^2$		
$Z_4^{-2}(x, y)$	13		$8yx^3 + 8y^3x - 6yx$		
$Z_4^4(x, y)$	14		$x^4 - 6y^2x^2 + y^4$		
$Z_4^{-4}(x, y)$	15		$4x^3y - 4xy^3$		

Figure 2-1: The first 15 Zernike Polynomials in Cartesian coordinates.[5]

The field distribution of a plane wave $A(x)$ at the pupil, for which the amplitude is A and

the phase aberration is $\phi(x)$, at the focal plane can be described as

$$A(u, v) = \frac{e^{\frac{ik}{2f}(u^2+v^2)}}{i\lambda f} \iint_{R^2} A(x)P(x)e^{-i\frac{2\pi}{\lambda f}(xu+yv)} dx, \quad (2-6)$$

with pupil function

$$P(x) = \begin{cases} 1 & \text{inside the lens} \\ 0 & \text{elsewhere} \end{cases} \quad (2-7)$$

Then by calculating the intensity of the field in the imaging plane, the image of the point source can be obtained.

$$I(u, v) = \frac{A^2}{\lambda^2 f^2} \left| \iint_{R^2} e^{-i\phi(x)} P(x) e^{-i\frac{2\pi}{\lambda f}(xu+yv)} dx \right|^2. \quad (2-8)$$

The image of the point source in the image plane is not a point. In the aberration-free system, the image of the point source is a bright central region together with the concentric rings around it. This pattern is called Airy Disk caused by the diffraction limit. If the aberration is considered, the image of the point source is not the Airy Disk. The example of the image of the point source with different aberrations are shown in Figure 2-1. The image of the point source is called PSF, which describe the response of the imaging system to a point source.

As the object can be seen as the collection of a set of independent point sources, the image is the combination of the images of each point. Then the image can be seen as the convolution of the object and the PSF:

$$i = o * h + n, \quad (2-9)$$

where i is the acquired image, o denotes the object, h refers to the PSF, and n is the additional noise.

The resolution of the image system depends on the width of the PSF. The resolution of an optical system refers to the shortest distance between two points in the object which can still be distinguished as two independent entities in the image plane. In 1873, German scientist Ernst Abbe found the resolution of an microscope is limited by the diffraction limit [17]. In theory, the minimum resolvable distance for an aberration free system is

$$d = \frac{\lambda}{2NA}, \quad (2-10)$$

where λ is the wavelength of the light, NA is the numerical aperture which is a number describing the amount of light that can be collected by the objective.

In practice, due to the inevitable aberration of the imaging system, the resolution is lower than the diffraction limit. The commonly used measure to characterize the resolution is Full Width at Half Maximum (FWHM): the width of the PSF measured at the level where the intensity is half of the maximum (Shown in Figure 2-2).

2-2 Super Resolution Technique

Super resolution technique is a set of methods which are used to break the diffraction limit of the optical system and enhance the resolution of the imaging system.

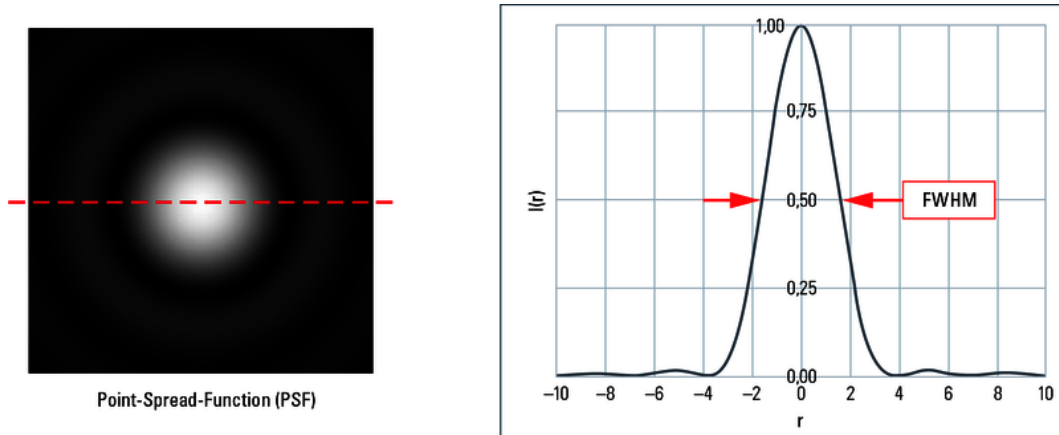


Figure 2-2: Left: The Point spread function of a system. Right: The cross-section plot of the PSF. ([6])

4Pi and I⁵M

Both 4Pi and I⁵M are the interference-based techniques which improve the axial (z-) resolution by introducing two opposing object lenses [18, 19].

The idea of the 4Pi laser scanning fluorescence microscope which improves the axial resolution by increasing the acceptance solid angle of the aperture was first proposed by the S. Hell in 1990. Four years later, he made this proposal come true [20]. A scheme diagram of 4Pi microscope is shown in Figure 2-3. The detected light of the detector are the combination of

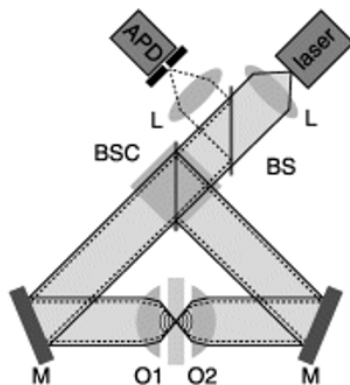


Figure 2-3: Optical scheme in 4Pi microscope [7]

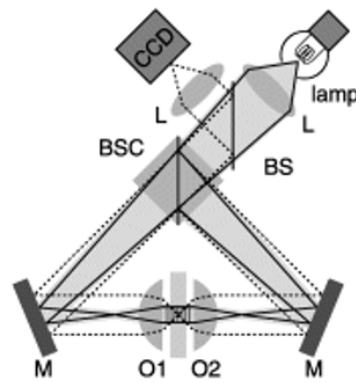


Figure 2-4: Optical scheme in I⁵M microscope [7]

the emitted light collected by two opposing object lenses, which are from the same Fluorescent molecule excited by the coherence beams. In the ideal situation, the solid angle of the light that an object lens can collect is 2π . Therefore, by using two opposing object lenses, the solid angle of the system is increased to 4π , in other words, the numerical aperture is increased. However, in practice, the numerical aperture of one object lens can only reach 1.3π , as a result the resolution can be improved from 500-700nm to 100-150nm. This kind of microscope is always used with STED together to realize the resolution optimization in 3-D problem.

The image scheme of I^5M is similar to 4Pi (see Figure 2-4). Instead of using the laser, the incoherent light source is used in I^5M . The I^5M is a combination of the I^2M and I^3M . I^2M , image interference microscopy, collects the confocal fluorescence lights illuminated by beams through two high numerical aperture and then interference of these lights is created on the CCD plane. The incoherent light can also be used to illuminate the sample. If we used the I^2M microscope in this way, it becomes I^3M , incoherence interference illumination microscopy, which can get the incoherence pattern of the sample. Gustaffson and his colleagues developed the I^3M and make a combination of these two techniques, then the I^5M is formed. During the measurement, a set of images can be obtained by scanning the focal plane of the sample layer by layer, and then using the proper deconvolution method to process the data, a high-resolution 3-D image is achieved. The resolution of the I^5M can reach 100nm [21]. Figure 2-5 shows the image deconvolution in both the 4Pi and I^5M .

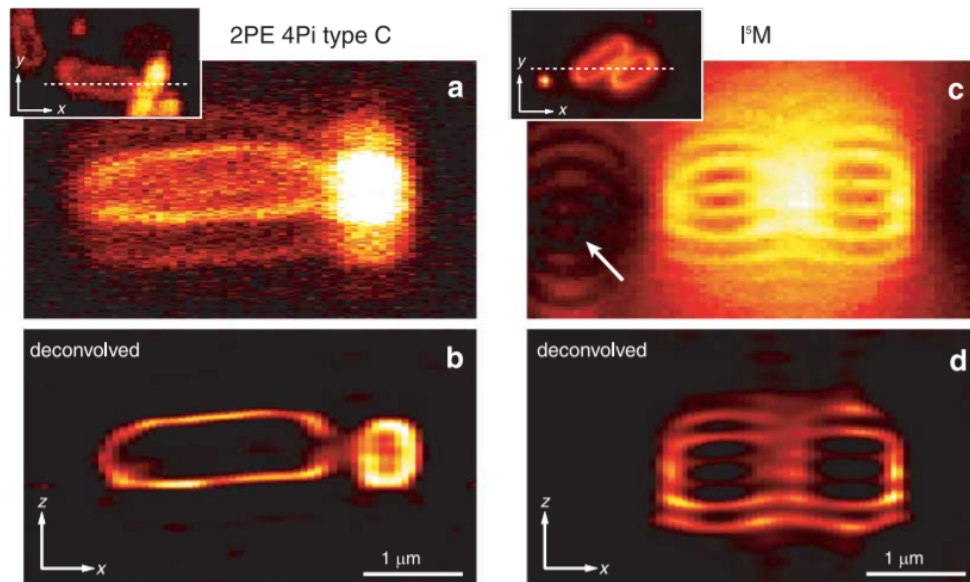


Figure 2-5: The axial slice in 4Pi and I^5M . (a) shows the typical section of the 3D image recorded by the 2PE PI of type C. The dashed line in the inset of figure (a) illustrate the position of xz-slice in the xy-overview. Figure (c) shows the deconvolution result of the figure (a). Figure (c) and (d) shows the recorded image and the deconvoluted image in I^5M . The inset of the figure (c) shows the position of xz-slice in the xy-overview. [7]

Stimulated emission depletion (STED) microscopy

The theory of the STED microscopy is first proposed by Stephen Gull et al. in 1994 [22] and then demonstrated by the biological experiment in 1999 [23].

As shown in Figure 2-6, two pulse lasers, of which one is for the excitation of the fluorescence molecules and the other one is for the depletion of the excited fluorescence molecules, are used. After exciting the fluorescence molecules by the first laser, the second laser, whose cross section is hollow, like a doughnut, is illuminated onto the same region as the first one. The fluorescence in the hole part of the second laser is still excited while the excited

fluorescence molecules outside the hole change to the ground state which can not be detected. Thus, an Airy disk is modified to a small bright spot. This kind of microscope is always used with 4Pi and I⁵M together, and the resolution of the STED microscope can reach 30nm. Figure 2-7 shows the image in both the confocal microscopy and the STED microscopy.

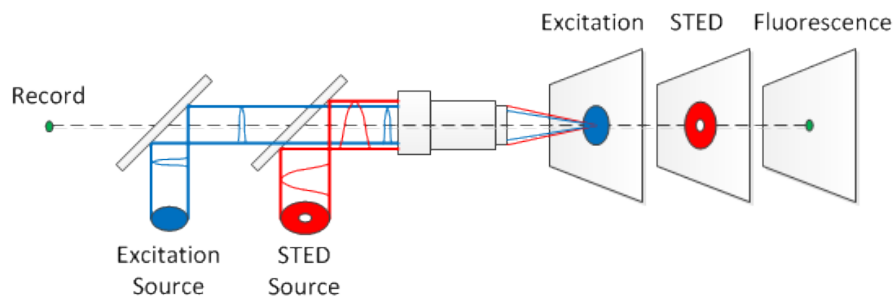


Figure 2-6: Optical scheme in STED [8]

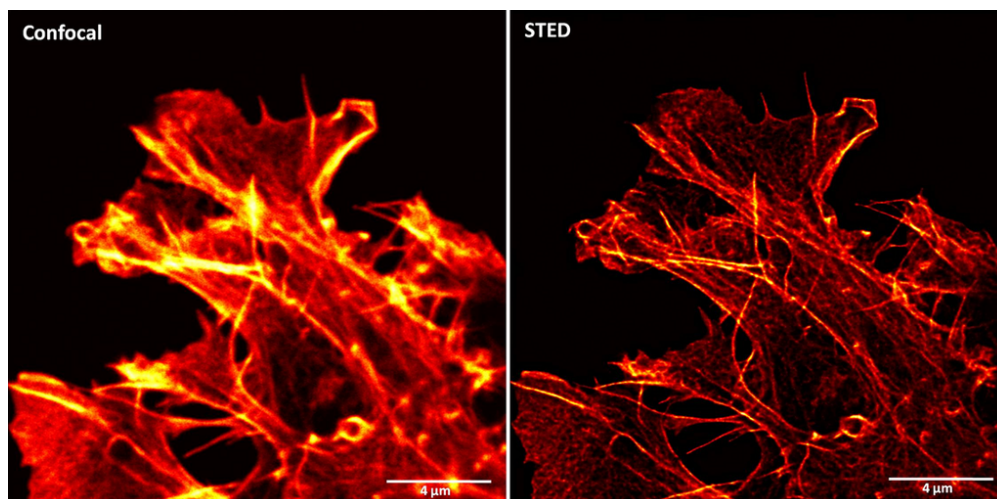


Figure 2-7: Fluorescent nanoparticles imaged by confocal microscopy (left) and STED microscopy (right) [9].

Single-molecule localization microscopy (SMLM)

The image of the fluorophore is broadened by the diffraction, which makes the fluorophores in the image plane are too close to resolve. But the broaden of the image does not have impact on the relative position of the image center of each fluorophore [24]. Based on this property, the SMLM technique are developed. Figure 2-8 illustrates the principle of the SMLM. Instead of imaging all the fluorophores together, the SMLM technique image the individual fluorophore in the object at a time and get the position of it. After getting the location of all fluorophores, the super resolution image can be constructed by plotting points at the corresponding positions.

In order to obtain the individual iamge of each fluorophore, the photoactivatable fluorophores are used. This kind of fluorophores can be activated by the laser and will return to the ground

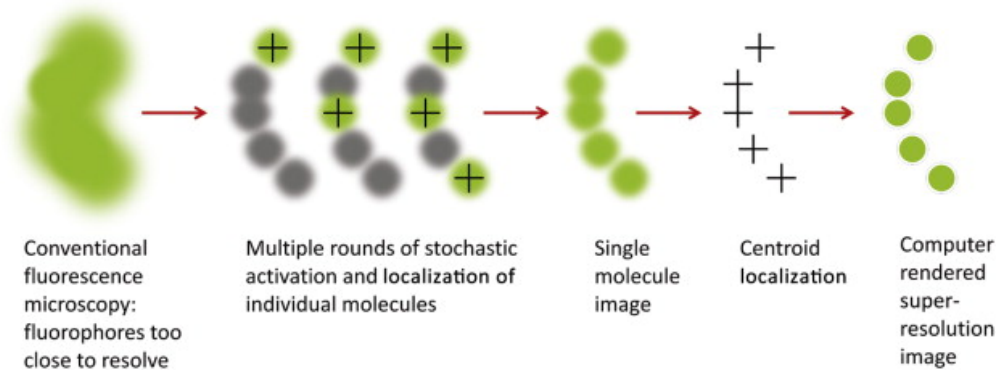


Figure 2-8: The process of super resolution imaging in SMLM [10]

state after emitted fluorescence for a short while. With the use of low intensity laser, although all the object is illuminated, only one or a few of fluorophores are activated. Each time the fluorophore in the object is activated randomly. By illuminating the object for plenty of times to make sure that each fluorophore has been activated at least once [24].

The most popular microscopes of SMLM are photoactivated localization microscopy (PALM) proposed by Betzig et.al [25] in 2006 and stochastic optical reconstruction microscopy (STORM) proposed by X. Zhuang [26] at the same time. The resolution of PALM and STORM are 20-30nm and 10-20nm respectively. Figure 2-9 shows the comparison of the image in confocal microscopy and the PALM.

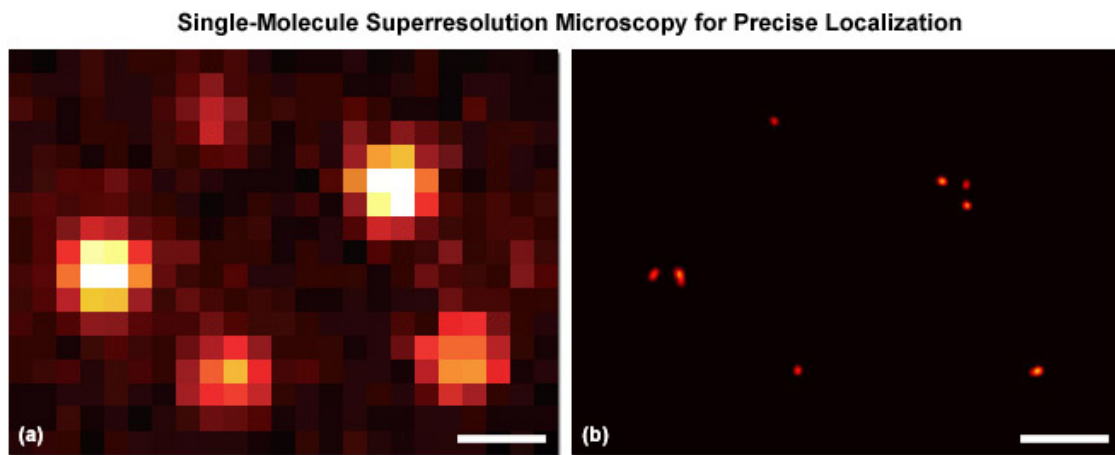


Figure 1

Figure 2-9: The image of confocal microscopy (left) and photoactivated localization microscopy (right) [11]

Structured illumination microscopy (SIM)

Structured illumination microscopy (SIM) is compatible with any fluorescence microscopes which puts a diffraction grating on the path of the laser beam. It uses spatial harmonics as periodic illumination pattern. It is a super-resolution imaging technique using moire effect

to shift the high spatial frequency information of the object into the pass-band of the optical transfer function. By separating these superimposed information components and shifting them to their original location in Fourier space, the resolution of this system is enhanced. The quality of the image depends on the thickness of the diffraction grating, the thinner the diffraction grating is, the higher quality the image have. The resolution of SIM can reach 100nm, the 2-fold higher resolution of the conventional microscope. The Figure 2-10 demonstrates how the SIM achieves the super resolution imaging and Figure 2-11 shows the comparison between the SIM and conventional side-field microscope imaging.

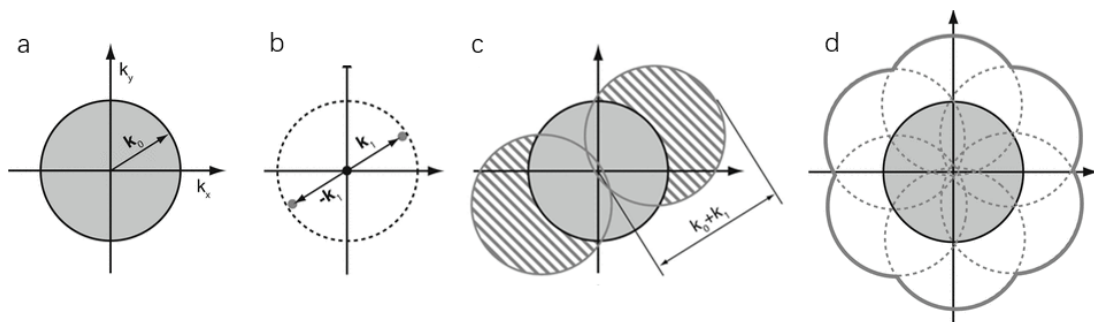


Figure 2-10: The principle of resolution improvement in structured illumination microscopy. (a) The support region of optical transfer function which is the observable region of the conventional microscope in Fourier domain. The three dots in (b) describes three information component. After getting the shifting-phase, these superimposed components can be shift back to their original position resulting in an expanded observable region (c). Rotate the illumination in three orientations to expand the resolution isotropically. [12]

2-3 The principle of SIM

Structured illumination microscopy (SIM) is a super resolution method which breaks the diffraction limit of the optical system and increases the spatial resolution of the wide-field fluorescence microscopy by using spatial structured illumination light [27, 28, 29]. Unlike other super resolution techniques, like PALM and STED, which improve the resolution by optimizing the modulation method of the PSF, the SIM achieves the super-resolution by obtaining the information outside the observed region in the frequency domain [30]. Compared with other super resolution techniques, SIM has several advantages, such as the fast rate of imaging, the compatibility with other optical systems, and the observation of the living cell, which make it widely used in medicine, biology.

In SIM, the sample is illuminated by the periodic light patterns which are created by the optical grating or digital micro-mirror device (DMD) [30]. After illuminated by the periodic light patterns, the high frequency information of the sample is down-modulated to the support area of the OTF, where the images of these information can be captured by the microscope. Since both the high frequency information and the low frequency information are modulated to the support area of the OTF, these information components are superimposed. The super-resolution is achieved by separating these information components and shift them back to their original position in the Fourier domain.

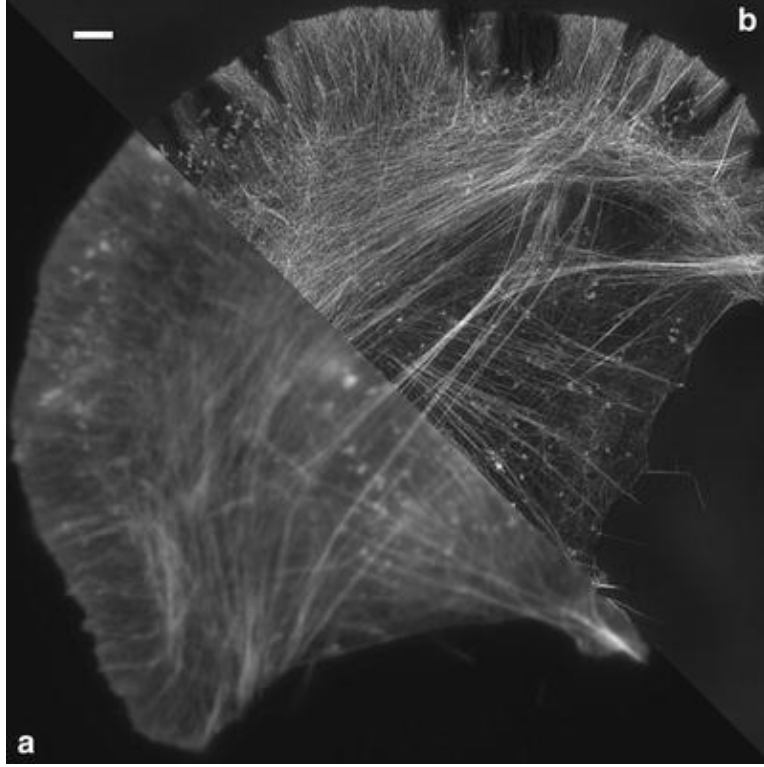


Figure 2-11: The image of the conventional wide-field microscope (a) and the SIM (b). [12]

The mathematical model of the image formation and image reconstruction of SIM are introduced below. The introduction of the image formation and the image reconstruction of SIM in this section are based on the principle described by Wicker *et al.* in [27, 31] as well as the method present by Lahrber *et al.* in [32], and the same notations are used.

2-3-1 Image Formation and Reconstruction in SIM

The SIM is characterized by the use of illumination patterns. The acquisition of several images for different illumination patterns is required to reconstruct the super resolution image. The periodic illumination pattern used in SIM is a set of spatial harmonics, and the illumination intensity can be expressed as:

$$I(\vec{r}) = \sum_{m=-M}^M a_m \exp\{i(2\pi m\vec{p} \cdot \vec{r} + m\phi)\}, \quad (2-11)$$

in which \vec{r} is the vector in spatial coordinate, a_m is the strength of the m^{th} harmonic, M denotes the number of the harmonics, \vec{p} represents illumination spatial frequency, i is the imaginary unit and ϕ is the phase of this illumination. For 2-D problem, in principle illumination patterns with 3 orientations which has three different phases are sufficient.

The observed image of a given fluorescent object is determined by three factors, the distribution of the fluorescent molecules on the object, the intensity of illumination patterns and the

PSF of the optical system. The relation among these three factors can be written as:

$$D(\vec{r}) = [S(\vec{r}) \cdot I(\vec{r})] \otimes h(\vec{r}), \quad (2-12)$$

where $S(\vec{r})$ is the sample fluorophore density, $h(\vec{r})$ is the point spread function. Therefore, the n^{th} SIM raw image captured in the imaging plane can be expressed as

$$D_n(\vec{r}) = \sum_{m=-M}^M [S(\vec{r}) a_m \exp\{i(2\pi m \vec{p} \cdot \vec{r} + m \phi_n)\}] \otimes h(\vec{r}). \quad (2-13)$$

Fourier transforming Eq. (2-13) gives

$$\tilde{D}_n(\vec{k}) = \sum_{m=-M}^M \exp\{im\phi_n\} \underbrace{a_m \tilde{S}(\vec{k} - m\vec{p}) \tilde{h}(\vec{k})}_{=:\tilde{C}_m(\vec{k})}, \quad (2-14)$$

where $\tilde{\cdot}$ represent the Fourier transform of the function, $\tilde{D}_n(\vec{k})$ can be regarded as the n^{th} raw image and $\tilde{C}_m(\vec{k})$ denote the information component. The composition of these individual raw images denotes the image vector, and similarly, the composition of all information components denotes the component vector. Therefore Eq. (2-14) can be rewritten as

$$\vec{\tilde{D}}(\vec{k}) = \mathbf{M} \vec{\tilde{C}}(\vec{k}), \quad (2-15)$$

in which \mathbf{M} denotes the component mixing matrix and

$$\mathbf{M}_{nm} = \exp\{im\phi_n\}. \quad (2-16)$$

Assume that the pattern phases are known, then components can be separated.

$$\vec{\tilde{C}}(\vec{k}) = \mathbf{M}^{-1} \vec{\tilde{D}}(\vec{k}) \quad (2-17)$$

After getting the phase for each individual component, these information components can be shifted to the correct position in Fourier space.

To achieve the resolution enhancement of the reconstruction, a set of raw images from different orientations with different phases need to be acquired, which means the component separation need to be repeated for all orientations. Then the phase shift of all the components are known and these component can be shifted back to their original frequency in Fourier domain. Next, a weighted-averaging, generalized Wiener filter is used to recombine these information components together, leading to the estimation

$$\tilde{S}'(\vec{k}) = \frac{\sum_{q,m} \{a_m \tilde{h}^*(\vec{k} + m\vec{p}_q) \tilde{C}_{q,m}(\vec{k} + m\vec{p}_q)\}}{\sum_{q',m'} \left\{ |a'_{m'} \tilde{h}(\vec{k} + m'\vec{p}_{q'})|^2 \right\} + w}. \quad (2-18)$$

Recall that a_m is the strength of the m^{th} harmonic, \vec{p} refers to the illumination spatial frequency, \tilde{C} indicates the information component and w denotes the Wiener filter parameter which is a constant and the value of it is chosen empirically. The index q here is introduced to denote the shift orientation.

The noise suppression of the Wiener filter leads to the distortion of the deconvolution spectrum, due to the non-constant of the object spectrum. Therefore, an Apodization filter is introduced to suppress the distortion in the high frequency spectrum [33]. Then the reconstructed object can be expressed as:

$$\tilde{S}'(\vec{k}) = \frac{\sum_{q,m} \{a_m \tilde{h}^*(\vec{k} + m\vec{p}_q) \tilde{C}_{q,m}(\vec{k} + m\vec{p}_q)\}}{\sum_{q',m'} \{ |a'_{m'} \tilde{h}(\vec{k} + m'\vec{p}_{q'})|^2 \} + w} \tilde{A}(\vec{k}) \quad (2-19)$$

where $\tilde{A}(\vec{k})$ indicates the apodization filter which prevents the ring artifact in the restored image by shaping the overall spectrum [32].

There are different shapes for the apodization filter. One of the effective apodization functions is given by the exponential function of the distance transform (s) of the footprint (f) of the normalized reconstructed OTF. And it is found that the 0.4-th power of the distance transform can achieve a good image restored result [31]. Figure 2-12 shows the cross-section plot of the apodization function.

$$\tilde{A}(\vec{k}) = [s(f(\tilde{h}(\vec{k})))]^{0.4}. \quad (2-20)$$

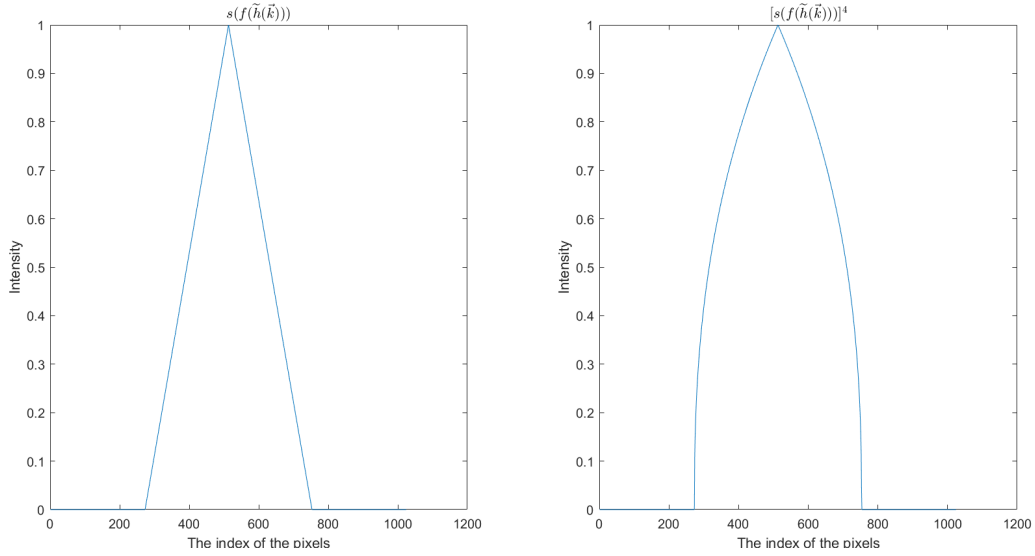


Figure 2-12: The cross-section plot of the distance transform result (left) and the Apodization filter (right).

2-3-2 Parameter estimation

The accurate estimation of the illumination pattern parameters is an important process in the SIM image reconstruction. With the proper parameters, the information components can be unmixed (Eq. 2-17) and the SIM orders can be shifted back to its original location (Eq. 2-19) in the Fourier domain. In the following subsection, the parameter determination method are introduced.

Phase shift estimation

To achieve the resolution improvement and get a high quality restored SIM image, the initial phase of each illumination pattern should be known with a high precision. The phase shift estimation algorithm used in this thesis is the non-iterative algorithm proposed by Wicker in [27], which using the auto-correlation of the filtered image spectrum at the spatial frequency \vec{p} to determine the phase. The filter here is the complex conjugated OTF, which is used to reduce the impact of the additional noise and the asymmetry of the OTF [27]. The filtered image is described by \tilde{D}'_n :

$$\tilde{D}'_n(\vec{k}) = \tilde{D}_n(\vec{k})\tilde{h}^*(\vec{k}). \quad (2-21)$$

Then the auto-correction (\otimes) of \tilde{D}'_n is calculated and we get

$$\mathcal{D}_n = [\tilde{D}'_n \otimes \tilde{D}'_n](\vec{p}) \quad (2-22)$$

The result of the Eq. 2-22 is a positive and complex value. Then the phase of the n^{th} image can be derived from the angle of this value, thus:

$$\phi_n = -arg\{\mathcal{D}_n\}. \quad (2-23)$$

Spatial frequency estimation

The use of the non-iterative phase estimation algorithm requires the precise known spatial frequency \vec{p} of the illumination pattern (See Eq. 2-22). The spatial frequency of the illumination pattern is estimated from the Fourier spectrum of the images. By finding the position of the peaks in the Fourier spectrum, the information of the spatial frequency can be obtained. The precision localization of this peaks do not only have impact on the estimation spatial frequency but also influence the accuracy of the phase shift estimation. A subpixel peak detection method presented in [32] is used in this work.

The estimation of the spatial frequency starts with the localization of the peaks in $\tilde{D}(\vec{k})$. The indices of these peaks are (u_0, v_0) in Fourier domain and the localization precision of these indices equals to the step size $\frac{1}{N_{x,y}}$, where $N_{x,y}$ is the length of the image. Next, an area around the corresponding pixel of this peaks in the spatial domain are selected and oversampling is done for this selected area [34, 35] (cited in [32]). Then the Fourier transform for this region is calculated using the twofold matrix multiplication:

$$\tilde{D}(\hat{u}, \hat{v}) = exp\left(\frac{-2\pi i}{N_y}\hat{v}^T y\right) D(x, y) exp\left(\frac{-2\pi i}{N_x}x^T \hat{u}\right) \quad (2-24)$$

where $exp(\cdot)$ refers to the exponential of each element of the input array, (x, y) is the coordinate in the spatial domain, and (\hat{u}, \hat{v}) is the indices of the subpixel after oversampling which around the original peak (u_0, v_0) . The use of this method can reduce the error of the localization of the peak, which is illustrated in Figure 2-13. After the oversampling, the detected location of the peak is closer to the actual position (see Figure 2-13(d)).

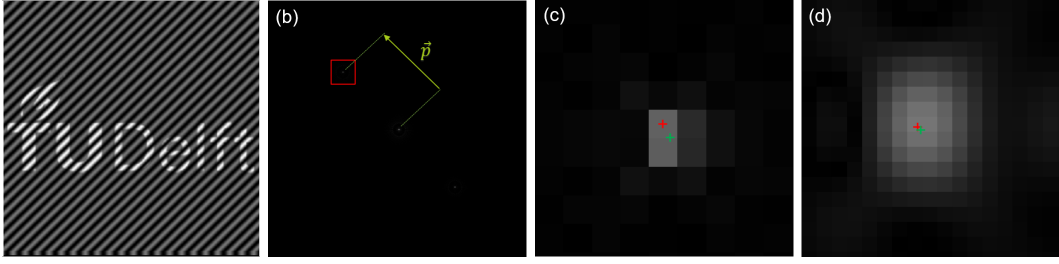


Figure 2-13: Illustration of the subpixel detection. (a) and (b) are raw image and its Fourier spectrum respectively. The wave vector is shown in (b). (c) shows the peak location mismatch, the green and red cross in (c) indicate the actual location and the location estimated with the original image. (d) shows the result of the proposed subpixel detection method.

Modulation strength calculation

After getting the spatial frequency \vec{p} and the initial phase ϕ as well as the OTF \tilde{h} , the modulation strength can be calculated from the OTF corrected information component directly [32]. The OTF corrected information component is obtained by:

$$\tilde{C}'_m = \frac{\tilde{C}_m \tilde{h}^*}{|\tilde{h}|^2}, \quad (2-25)$$

where $*$ represent the complex conjugated. Then the strength of the m -th harmonic is determined by:

$$a_m = \left| \frac{\sum_{\vec{k}'} \tilde{C}'_0^*(\vec{k}') \tilde{C}'_m(\vec{k}' + m\vec{p})}{\sum_{\vec{k}'} |\tilde{C}'_0(\vec{k}')|^2} \right|, \quad (2-26)$$

where \vec{k}' is the overlapping region of the \tilde{C}'_0 and $\tilde{C}'_{\pm 1}$ (shown in Figure 2-14), $|\cdot|$ refers to the absolute value.

2-4 Summary

In this chapter, the introduction of both the basic concept of the optical imaging and the principle of the super resolution technique have been made. As this thesis is focus on the SIM, the principle of the image formation and image restoration of the SIM system are described in detail. In the next chapter, we will talk about the TIP algorithm a novel blind image deconvolution algorithm.

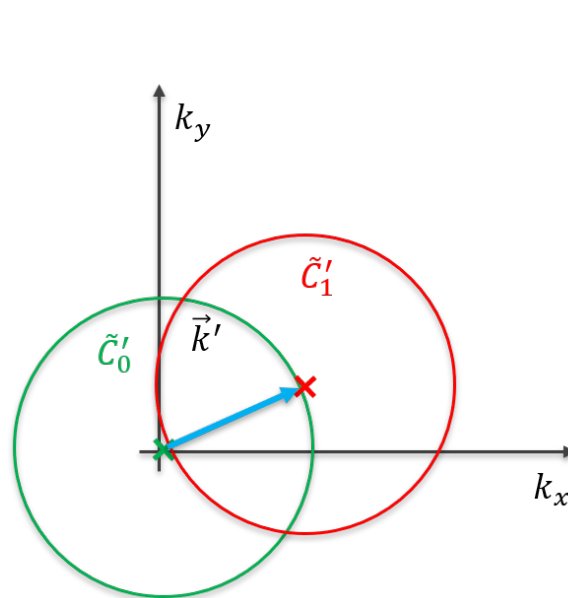


Figure 2-14: The overlapping spectrum. The blue arrow indicates the wave vector \vec{p} , by which the information component \tilde{C}'_1 is shifted back to its correct position. As shown, there is an overlap region. The two spectrum in this overlap region is differ by a complex number. When $a_0 = 1$, the absolute value of this complex number is the modulation depth (See Eq.2-26).

Chapter 3

TIP algorithm

In Chapter 2, the concept of the optical imaging is introduced. In practice, most of the time, the only thing we can obtain from an optical imaging system is the image. The PSF and the observed sample are always unknown, which make the image restoration a blind deconvolution problem. In this chapter, both the blind multi-frame deconvolution by tangential iterative projections [3] and the blind single-frame deconvolution by tangential iterative projections [4] developed by Wilding *et al.* are going to be explained in depth. The explanation of the TIP algorithm follows the reasoning in [3, 4] and the same notations are used.

Most of the current blind deconvolution algorithms are using the iterative method. Compared with the non-iterative method, the iterative blind deconvolution algorithms have higher efficiency in handling the large-scale problems and is more convenient to incorporate the known prior knowledge, like the non-negativity of both the object and the PSF [36]. The iterative blind deconvolution algorithm proposed by the Ayers *et al.* [37] is one of the typical method to solve the blind deconvolution problem. Starting with an arbitrary non-negative value of the image, this algorithm estimate the object and the PSF iteratively. After each iteration, zero is assigned to all the negative values in estimated object or PSF.

However, It is not possible to completely reconstruct an object with the Ayers's algorithm due to the spatial frequency loss caused by the aberration [3]. Therefore, a method by acquiring multi frame images with different aberrations is proposed. As not all the images suffer from the same aberration, if we have a sufficient image set, the object can be reconstructed completely and the PSF can be obtained. This method was first demonstrated by Schulz in 1993 [38], after a short while, Yaroslavsky and Caulfield also did the demonstration [39].

A multi-frame blind deconvolution is an ill-posed inverse problem which can be solved by minimize the following cost function [15] (cited in [3]):

$$\{\hat{h}_n, \hat{o}\} = \arg \min_{h_n, o} \sum_{n=1}^N \|i_n - o * h_n\|^2 + \lambda_o Q(o) + \lambda_h R(\{h\}), \quad (3-1)$$

recall that h_n describes the set of the PSF, o is the observed sample, i_n is the aquired images, λ_o and λ_h are the coefficient which are used to get a trade-off between the regularization terms

and the fidelity of the reconstruction as well as the $Q(o)$ and $R(\{h\})$ are the regularization terms for object and PSF respectively.

The implementation of the blind deconvolution can be solved using the alternative minimization framework, where the problem is split into two sub-problems, the 'o-step' and 'h-step':

$$\text{"o - step"} : \hat{o}^{k+1} = \min_o F(o, \{h_n^k\}) + Q(o) \quad (3-2)$$

and

$$\text{"h - step"} : \{\hat{h}_n^{k+1}\} = \min_{h_n} F(o^{k+1}, \{h_n\}) + R(\{h_n\}), \quad (3-3)$$

where F represents the formulation $\sum_{n=1}^N \|i_n - o * h_n\|^2$ which is the loss of the system and Q and R are regularization terms. For each step either the PSF h or the object distribution o is fixed, which makes the problem a standard non-blind deconvolution problem. By calculating the global minimization of each sub-problem in each iteration, the global minimization of the original function Eq. 3-1 which contains two unknown parameters, will be reached after several iteration[15, 40]. However, the implementation of the regularization term will increase the computational complexity and the incorrect parameters will lead to the blind deconvolution algorithm converging to a wrong result.

3-1 Multi-frame TIP

Wilding *et al.* propose a noise robust, quick multi-frame blind deconvolution framework, called blind multi-frame deconvolution by tangential iterative projections (TIP), which do not require the implementation of regularization terms. The cost function of multi-frame TIP deconvolution describe in [3] is:

$$\arg \min_{H_n, O} \sum_{n=1}^N \|I_n - O \cdot H_n\|^2, \quad \text{s. t. } H_n \in \mathcal{H}, O \in \mathcal{O} \quad (3-4)$$

where, \mathcal{H} and \mathcal{O} are the constraints of the PSF and object respectively. The problem described in Eq. 3-4 is a non-convex problem which do not have an unique solution [40] (cited in [3]). The aim of the TIP is to use the simplest operation and the minimum prior information to get a close enough estimation of the object. TIP makes use of the alternative minimization framework. The input of the TIP algorithm is a set of images i_n with different PSFs h_n of the same object o . For the k-th iteration, the estimated object spectrum can be obtained by projecting the result of the linear deconvolution towards the feasible set of the object:

$$\tilde{O}^{(k)} = \frac{\sum_{n=1}^N I_n (\hat{H}_n^{(k-1)})^*}{\sum_{n=1}^N |\hat{H}_n^{(k-1)}|^2}, \quad n = 1, \dots, N. \quad (3-5)$$

Then the spectrum of the OTF can be obtained by:

$$\tilde{H}_n^{(k)} = \frac{I_n}{\tilde{O}_n^{(k)}}. \quad (3-6)$$

The linear deconvolution process shown in Eq. 3-5 and Eq. 3-6 is unconstrained, thus the result obtained from these functions may contain some unfeasible value. In order to remove

the unfeasible value in it, the projection process which project the linear deconvolution result into its feasible set is done. Then the estimated object spectrum becomes:

$$\hat{O}^{(k)} = \mathcal{P}_{\mathcal{O}} [\tilde{O}^{(k)}], \quad (3-7)$$

where $\mathcal{P}_{\mathcal{O}}$ is the projection operation of the object spectrum. Similarly, the estimated OTF also needs to be projected to its feasible set to get the feasible result with the projection $\mathcal{P}_{\mathcal{H}}$

$$\hat{H}_n^{(k)} = \mathcal{P}_{\mathcal{H}} [\tilde{H}_n^{(k)}]. \quad (3-8)$$

During the projection process, the PSF (or object) is calculated from OTF(or object spectrum) with the inverse Fourier transform. Physically, the intensity of the PSF (or the object) is non-negative and real. Therefore, only the real part of the inverse Fourier transform is taken and 0 is assigned to all the pixels in the object and PSF which having negative value.

The flowchart of this algorithm is shown in Figure 3-1. There are four steps in this flowchart. The \mathbb{X} defines the support size of the PSF which is a tunable area defined by user. The δ -function are assigned to the PSFs and used as the initial value of the PSF set. The description of each step is shown in Table 3-1

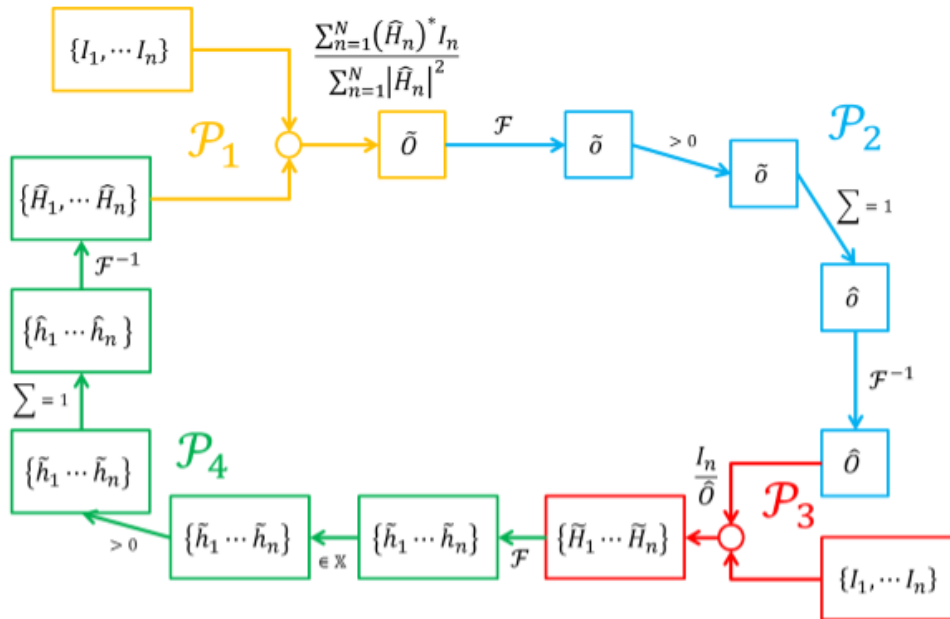


Figure 3-1: The diagram of the multi-frame TIP. This framework contains 4 steps. \mathcal{P}_1 and \mathcal{P}_3 are linear deconvolution. \mathcal{P}_2 and \mathcal{P}_4 are the projection to the feasible set \mathcal{O} and \mathcal{H} respectively [3].

3-2 Single-frame TIP

After a set of images of an object is obtained, using multi-frame TIP framework, the PSF set and the object can be restored. However, this framework only works with the multi-frame problem due to the limit prior information in the single-frame image [3]. Thus, this

Step/Projection	Process	Description
Step 1 — \mathcal{P}_1	$\tilde{O} = \frac{\sum_{n=1}^N (\hat{H}_n)^* I_n}{\sum_{n=1}^N \hat{H}_n ^2}$	Multi-frame linear deconvolution
Step 2 — \mathcal{P}_2	$\hat{o} = \mathcal{F}\{\tilde{O}\}$	Fourier Transform
	$\tilde{o} = 0, \text{ if } \hat{o} \leq 0$ $\sum \tilde{o} = 1$	Non-negativity Threshold Normalisation
	$\hat{O} = \mathcal{F}^{-1}\{\tilde{o}\}$	Inverse Fourier Transform
Step 3 — \mathcal{P}_3	$\tilde{H}_n = \frac{I_n}{\hat{O}}$	Single-frame linear deconvolution
Step 4 — \mathcal{P}_4	$\hat{h}_n = \mathcal{F}\{\tilde{H}_n\}$	Fourier Transform
	$\tilde{h}_n = 0, \text{ if } x \notin \mathbb{X}$	Finite Support Constraint
	$\tilde{h}_n = 0, \text{ if } \tilde{h}_n \leq 0$ $\sum \tilde{h}_n = 1$	Non-negativity Threshold Normalization
	$\hat{H}_n = \mathcal{F}^{-1}\{\tilde{h}_n\}$	Inverse Fourier Transform

Table 3-1: The description of each step of the TIP algorithm [3]

framework is not suitable to estimate the PSF of a blurred image. Later, some modifications to this algorithm were done by Wilding, and the algorithm works on the single-frame problem [4].

The idea of the single-frame TIP comes from the multi-frame TIP. The single-frame image can be converted into multi-frame image by splitting it into several patches, which take place of the multi-frame input images. These patches are labeled with i_p of which the corresponding object is represented by o_p . Assume the isoplanatic imaging condition, the PSF h of all these patches are the same. Then the cost function of this problem becomes:

$$\arg \min_{H, O_p} \sum_{p=1}^{P^2} \|I_p - O_p * H\|^2, \quad \text{s. t. } H \in \mathcal{H}, O_p \in \mathcal{O}, \quad (3-9)$$

where \mathcal{H} and \mathcal{O} are the constraints of the PSF and object respectively. In this case, the patches can be considered as the images of different objects convolved with a time-invariant PSF. Compared with the case described in [3] that the images are the convolution result of the constant object and different PSFs, the role of the PSF in the SF-TIP is the same as the role of the object in the MF-TIP. Similarly, the role of the object in SF-TIP is the same as the PSF in the MF-TIP.

Mathematically, if the same constraint is used in the algorithm, the idea that estimate the object based on a set of images with different PSFs and the idea which find the PSF with a set of images from different objects is equivalent. The patches I_p used in SF-TIP are created by masking the image i with several non-binary masks m_p in spatial domain (see Figure 3-2), thus $I_p = I \star M_p$, in which M_p is the Fourier transform of the m_p and $*$ is the convolution operator. The performance of the algorithm is influenced by the choice of the non-binary mask, as the non-binary mask will decide the regions of the image which are used as the input. A good non-binary mask can lead to $O_p \approx O * M_p$. Hence, acquiring the image of multiple objects can be replaced by splitting one image into several patches.

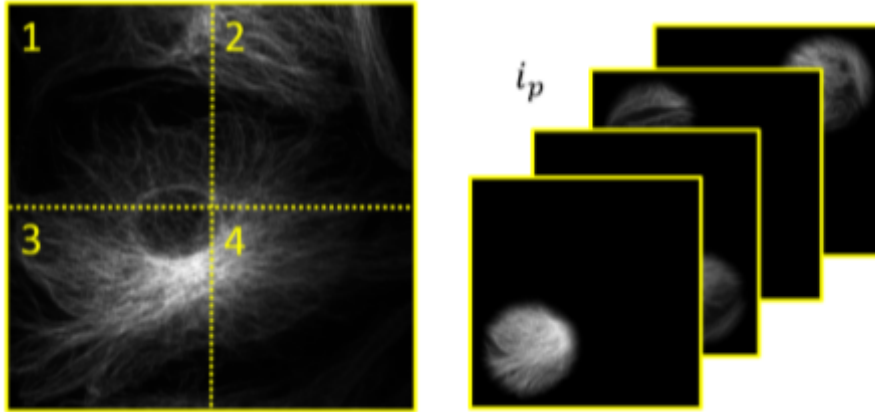


Figure 3-2: The illustration about how to split the single-frame image into several patches [4].

The SF-TIP start with the linear deconvolution of the OTF:

$$H^{(k)} = \mathcal{P}_{\mathcal{H}} \frac{\sum_{p=1}^{p^2} I_p \cdot \hat{O}_p^{(k)}}{\sum_{p=1}^{p^2} |\hat{O}_p^{(k)}| + \epsilon}. \quad (3-10)$$

Then the object spectrum can be obtained by

$$\begin{aligned} O_p^{(k)} &= \mathcal{P}_{\mathcal{O}} \frac{I_p}{H^{(k)}}. \\ &= \mathcal{P}_{\mathcal{O}} \frac{I * M_p}{H^{(k)}} \end{aligned} \quad (3-11)$$

Figure 3-3 shows the steps of the single-frame TIP, and the description of these step are shown in Table 3-2. The SF-TIP algorithm also requires the user-defined support size of PSF, which need to be tuned carefully.

3-3 Summary

In this chapter, the TIP algorithm is discussed in depth. The TIP algorithm works on both the single-frame and multi-frame scenarios. The process of the TIP algorithm follows the scheme of the alternative minimization. The algorithm works in both the Fourier domain and the spatial domain. The support constraint is implemented in the spatial domain, to remove the unrealistic data. The basic constraint in the TIP algorithm for both the PSF and object are the non-negative and real.

The TIP algorithm hasn't been applied to the SIM image deconvolution before. Whether this algorithm is suitable for the PSF estimation of the SIM images is not known. In the next chapter, how to implement the TIP algorithm in the SIM will be shown and the performance of the TIP algorithm in SIM will be analyzed.

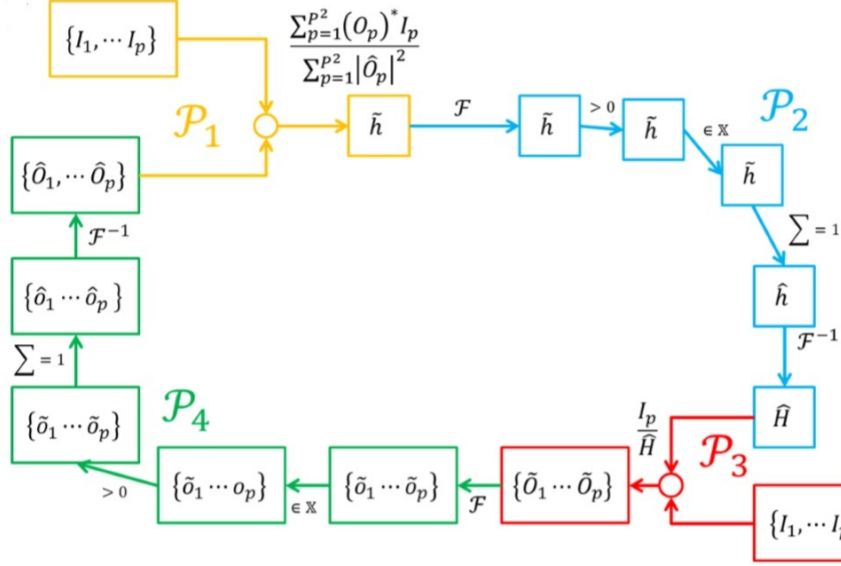


Figure 3-3: The diagram of the single framework. This framework contains 5 steps. The first one is the image preparation while the other four steps are the projection steps. \mathcal{P}_1 and \mathcal{P}_4 are linear deconvolution. \mathcal{P}_2 and \mathcal{P}_3 are the projection to the feasible set \mathcal{H} and \mathcal{O} respectively [4]

Step/Projection	Process	Description
Step 1— Preparation	$I. * Mask_p$	split images into patches
Step 2— \mathcal{P}_1	$\tilde{H} = \frac{\sum_{p=1}^N (\hat{O}_p)^* I_p}{\sum_{p=1}^N \hat{O}_p ^2}$	multi-frame linear deconvolution
Step 3— \mathcal{P}_2	$\tilde{h} = \mathcal{F} \{ \tilde{H} \}$	Fourier Transform
	$\tilde{h} = 0$, if $h \leq 0$	Non-negativity Threshold
	$\sum \tilde{h} = 1$	Normalisation
	$\hat{H} = \mathcal{F}^{-1} \{ \tilde{h} \}$	Inverse Fourier Transform
Step 4— \mathcal{P}_3	$\tilde{O}_n = \frac{I_p}{\hat{H}}$	Single-frame linear deconvolution
Step 5— \mathcal{P}_4	$\hat{o}_n = \mathcal{F} \{ \tilde{O}_n \}$	Fourier Transform
	$\tilde{o}_n = 0$, if $x \notin \mathbb{X}$	Finite Support Constraint
	$\tilde{o}_n = 0$, if $\tilde{o}_n \leq 0$	Non-negativity Threshold
	$\sum \tilde{o}_n = 1$	Normalization
	$\hat{O}_n = \mathcal{F}^{-1} \{ \tilde{o}_n \}$	Inverse Fourier Transform

Table 3-2: The description of each step of single-frame TIP algorithm

PSF Estimation with TIP Algorithm in SIM

The ability that the TIP can retrieve the PSF and object from blurred images are discussed in Chapter 3. In this chapter how to implement the TIP in SIM will be discussed. According to the simulation of the SIM discussed in Appendix A, there are two type of images we can obtain from the SIM: the nine raw images and the wide-field image. Based on these two kind of images the method to implement the TIP deconvolution algorithm in SIM is divided into two types. The first one is the multi-frame TIP with the SIM raw images, the second one is the single-frame TIP with the wide-field image.

4-1 TIP with raw images

According to Chapter 2, the obtained images of SIM before being processed with a specialized algorithm are the nine raw images of which the high-frequency information are not in their proper position. The image formation can be considered as the convolution between the PSF and the dot-product result of the object and the sinusoidal illumination patterns (Eq. 2-12). Therefore, the formation of the n^{th} raw image can be written as:

$$D_n = (S \cdot I_n) * h + m, \quad n = 1, \dots, 9, \quad (4-1)$$

where D_n is the n -th raw image, I_n is the corresponding sinusoidal illumination pattern, S is the observed sample, h is the PSF, and m is the Poisson noise. If the illuminated sample is considered as a single unit which means the term $S \cdot I_n$ is considered as a single unit, the nine raw images of the SIM can be regarded as the images of different objects. To simplified the expression below, the illuminated object $D \cdot I_n$ is replaced by W_n , then the Eq.(4-1) can be rewritten as:

$$D_n = W_n * h + m., \quad n = 1, \dots, 9 \quad (4-2)$$

Therefore the problem here becomes how to retrieve a constant PSF from the images of a set of objects. Compared with the MF-TIP algorithm introduced in 3, which aims to retrieve the

unknown object from a set of images generated with different PSFs, the role of the PSF and object in the problem described by Eq. (4-2) are reversed. The simple linear deconvolution among the objects and the images cannot get an effective PSF estimate. Like the MF-TIP algorithm, the finite support region is also needed in this case to make the solution convergent. Mathematically, if the constraints used here are the same as the constraints used in multi-frame TIP algorithm in Chapter 3, the problem to restore the object from the images with multiple PSFs and the problem to retrieve the PSF from the image of multiple objects are equal. Therefore a multi-frame TIP algorithm can be implemented.

The flowchart of the algorithm is similar to the flowchart shown in Figure 3-1. The difference is that instead of doing the multi-frame linear deconvolution with image set and the PSF set, here the PSF set is replaced by the object set. Figure 4-1 is the flowchart showing the steps of the algorithm.

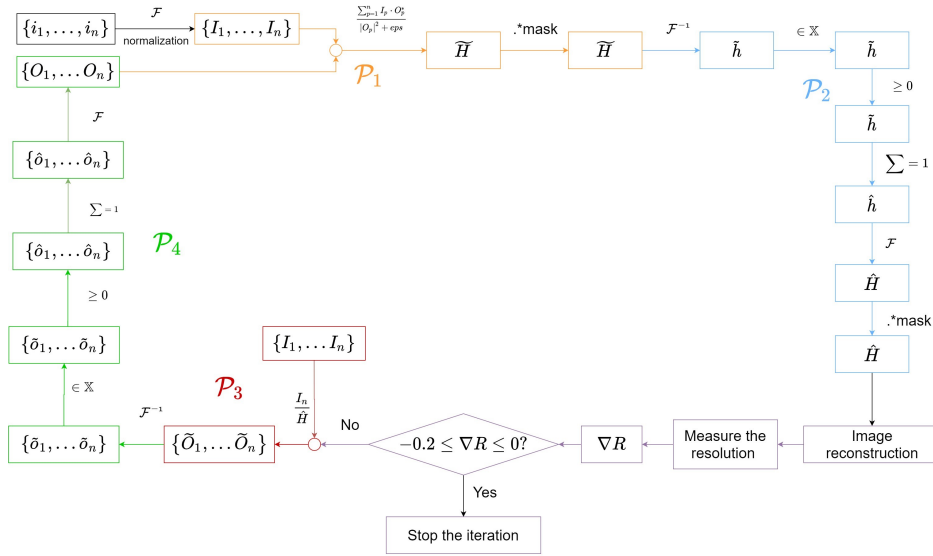


Figure 4-1: The flowchart of the MF-TIP algorithm in SIM. Four projection steps are shown in flowchart and the corresponding operations are shown by the lines between the boxes. \mathcal{P}_1 is the multi-frame linear deconvolution, \mathcal{P}_2 is the projection to the feasible set of the PSFs, \mathcal{P}_3 is the linear deconvolution for each frame, \mathcal{P}_4 is the projection to the feasible set of the object. ∇R is the first derivation of the resolution.

The algorithm starts with the normalization of the input images, and then an apodization window are implemented on these images, which is used to create a sharp edge of the images and reduce the edge effect of the Fourier transform. The δ -function is assigned to object as the initial value of it. The process of the main loop is described by 4 operators \mathcal{P}_1 , \mathcal{P}_2 , \mathcal{P}_3 and \mathcal{P}_4 . The purpose of these four steps are the same as the description in Table 3-2. In step \mathcal{P}_2 , a modification is introduced. A new constraint for the OTF which is described by *mask* in Figure 4-1 is introduced. This constraint will be discussed later in this chapter.

4-2 TIP with wide-field image

In SIM, except the 9 raw images, another type of image, the wide-field image, can be obtained. The wide-field image of SIM is the sum of the nine raw images, which can be described as:

$$D = \sum_{n=1}^9 (S \cdot I_n) * h + m. \quad (4-3)$$

Based on the distributivity of the convolution, the Eq.(4-3) can be rewritten as:

$$\begin{aligned} D &= \left(\sum_{n=1}^9 S \cdot I_n \right) * h + m \\ &= (S \cdot \tilde{I}) * h + m, \end{aligned} \quad (4-4)$$

where \tilde{I} is the sum of all illumination patterns. In this case, the problem becomes using single frame image to retrieve the object and the PSF, which satisfy the requirement of the single-frame TIP algorithm. The object will be retrieved here is the sum of all the illuminated samples $S \cdot \tilde{I}$.

The algorithm starts with multiplying the normalized image with several non-binary masks which are used to do the image-splitting and apodization. The split patches together with the δ -function (the initial value of the object) are used as the input of the main loop. The main loop of this algorithm contains 4 steps, two linear deconvolution and 2 projections. The framework of the SF-TIP algorithm which use the wide-field image to retrieve the PSF is similar to the framework shown in Figure 4-2. The difference is that an constraint for the OTF is introduced between the \mathcal{P}_1 and \mathcal{P}_2 .

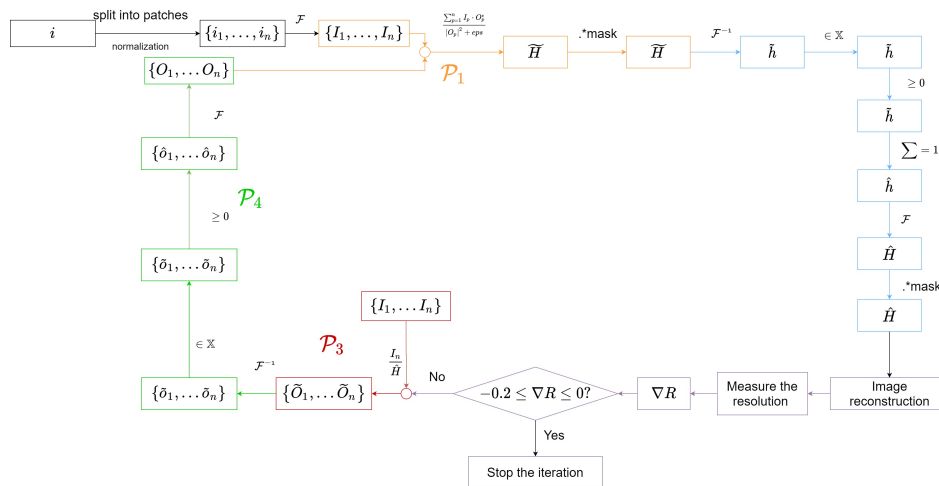


Figure 4-2: The flowchart of the SF-TIP algorithm in SIM . The image is first split into several patches to create the images for the different objects. Then the multi-frame linear deconvolution is done in the \mathcal{P}_1 . In \mathcal{P}_2 , the PSF estimate is projected to its support region to get the estimated PSF. Then the linear deconvolution is done in \mathcal{P}_3 . Finally, the projection process for the estimate object is done in \mathcal{P}_4 . ∇R is the first derivation of the resolution.

4-3 Constraints

In the chapter 3, the frameworks of both the SF-TIP and MF-TIP are introduced. Even though the cost function of the TIP is a non-convex function, by introducing the suitable projection constraints, a close enough object and PSF can be obtained. The main projection constraints \mathcal{P} used in the algorithm are:

- \mathcal{P}_o : $o(o \leq 0) = 0$. This constraint is defined based on the physical reality of the object that the intensity of an object is non-negative.
- \mathcal{P}_h : $h(h \leq 0) = 0$. This constraint remove all the negative value in the estimated PSF, since the negative value is physically impossible.
- \mathcal{P}_{Re} : $x = Re(\mathcal{F}^{-1}(X))$. During the projection process in the TIP algorithm, the inverse Fourier transform is done to calculate the object or the PSF from its Fourier domain counterpart. The result of the inverse Fourier transform contain complex values in it which is physically impossible. Therefore, only real values in the inverse Fourier transform result are taken. All the complex parts are removed.
- $\mathcal{P}_{norm}(h)$: $h = \frac{h}{\sum h}$. Normalized the PSF during the iteration, since the total intensity of the PSF is 1.

In an optical imaging system, based on the setup of this system, the diffraction limit of this system can be calculated. The ideal PSF of an optical system is the Airy disk caused by the diffraction limit. However, in practice, due to the aberration, the PSF is always larger than the ideal one in spatial domain. Thus, in Fourier domain, the diameter of the OTF is always smaller than the diameter of the diffraction limit OTF. Therefore, a new constraint is introduced in the Fourier domain.

- \mathcal{P}_H : $H(H \notin \mathcal{H}_{OTF}) = 0$, \mathcal{H}_{OTF} is the support region of the OTF generated based on the diffraction limit. In order to remove the high frequency disturbance in the OTF, a binary mask is created for which all the frequencies out of the support region of the OTF is set 0. The radius of the diffraction limit is calculated by Eq. 2-10, and then based on this radius, a circular mask is generated. The mask is shown in Figure 4-3. This mask can remove the out-of-band noise of the OTF, which has the impact on both the convergence rate and the convergence result. The use of this mask won't really help in the performance of the PSF estimation, but this mask can used to help find a proper stop criterion for the TIP algorithm, which will be discussed later in 4-4 Stop Criterion. The diffraction limit OTF is also tested here using as a support region for the OTF to remove the out-of-band noise and smooth the estimated OTF. However, it turned out that with the implementation of this kind of mask, the estimated OTF will converge to an incorrect result.

The performance of the PSF estimation can be described by the Peak Signal-to-Noise Ratio (PSNR) which is used in [4]. The higher the PSNR value is, the better the PSF estimate is. The PSNR can be obtained by:

$$PSNR = -10 \log_{10} \left\{ \frac{1}{N} \sum |h - \hat{h}^{(k)}| \right\}, \quad (4-5)$$

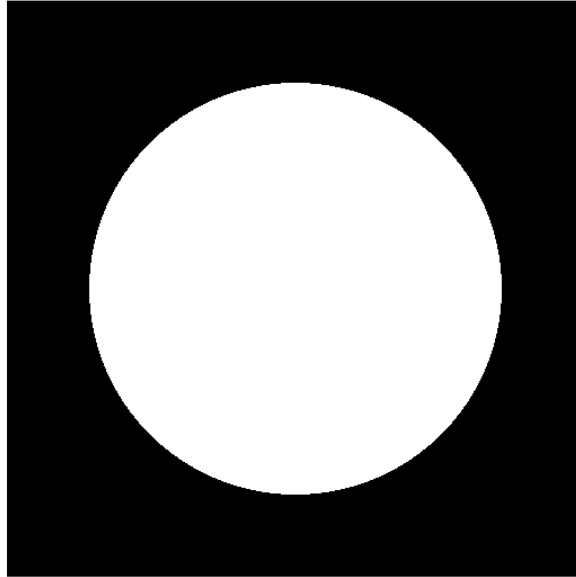


Figure 4-3: The binary mask generated based on the diffraction limit. The radius of this mask is $d = \frac{\lambda}{2NA}$

where N is the number of pixel in an image, h is the simulated PSF and $\hat{h}^{(k)}$ is the PSF estimate of the k -th iterations. The comparison of the PSNR curves for the estimated PSF with and without the binary mask are shown in Figure 4-4. According to the Figure 4-4, the PSNR of the TIP framework with the binary mask is more stable and have less fluctuation compared with the PSNR of the TIP framework without the binary mask, since the standard derivation of the former is smaller. However, the use of the binary mask reduces the convergence rate.

The PSNR shows how close the estimated PSF is to the actual PSF. In a noise-free condition, the quality of the restored image depends on the accuracy of the estimated PSF, thus the PSNR can be used to determine the quality of the restored image. But, in our case, the noise cannot be ignored, and the noise may introduce the error in the illumination pattern parameter estimation which will be finally reflected in the resolution of the restored image. To measure the relationship between the PSNR and the resolution of the restored image, for each iteration, the resolution of the image restored with the estimated PSF is calculated by measuring the Fourier ring correlation of that image which is introduced in Appendix C, and the result are shown in Figure 4-5. With the increase of the number of the iterations, the resolution of the restored image doesn't keep increasing. After several iterations, the resolution is nearly stable.

Due to the PSF estimate which has the highest PSNR may not be the PSF which can achieve the highest performance in the image reconstruction. To compare the performance of the different TIP frameworks, the distribution of the minimum resolution of the images restored from 160 image-PSF pairs with different aberration strengths in 100 iterations is drawn (Shown in Figure 4-6). According to the distribution shown in the Figure 4-6, the

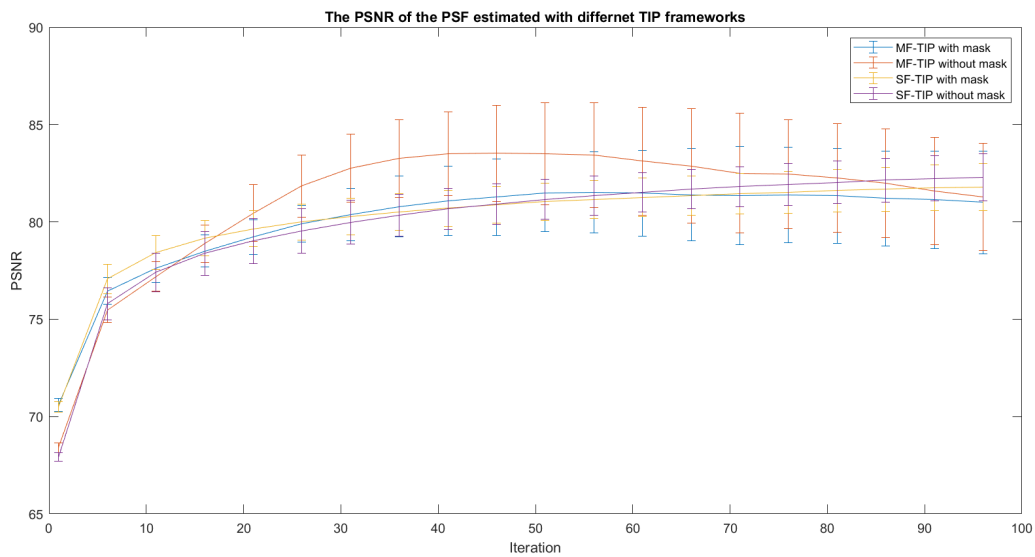


Figure 4-4: The mean PSNR of the PSF for 160 different image-PSF pairs deconvolved using the four TIP frameworks. The label of each curve are shown at the bottom right corner in the figure. The errorbar shows the standard derivation.

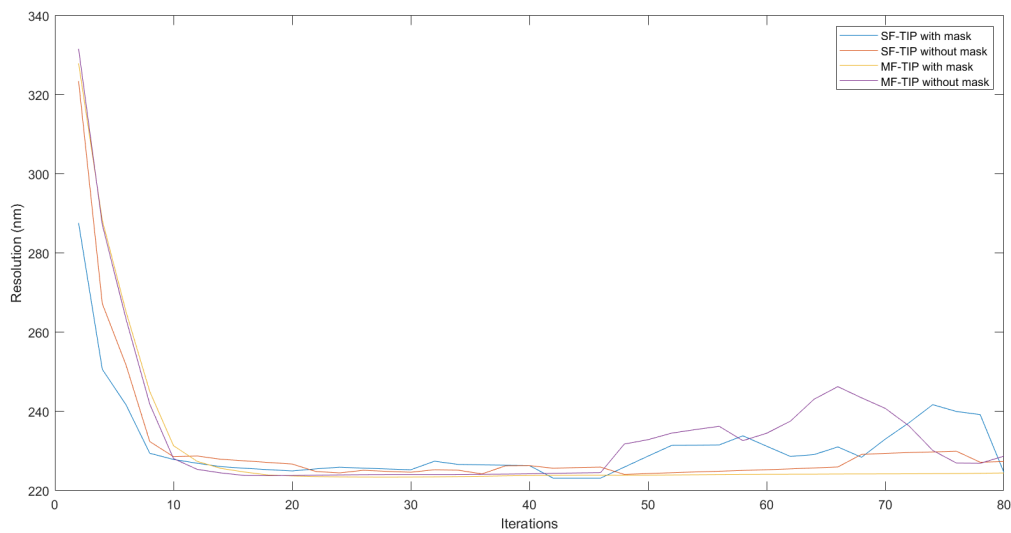


Figure 4-5: The relationship between the mean resolution and the number of iteration of the TIP algorithm.

performance of the four TIP frameworks are similar.

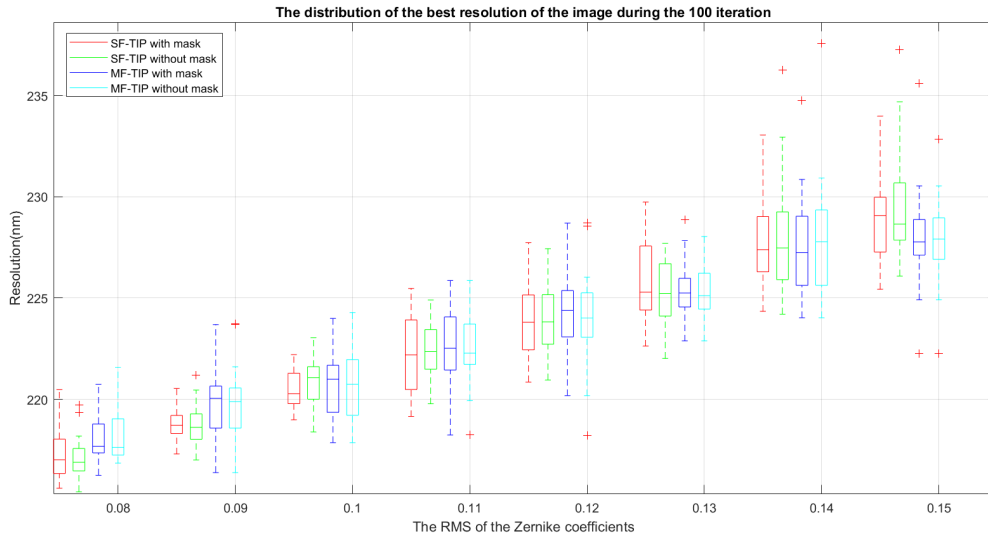


Figure 4-6: The distribution of the minimum resolution of the images restored from the 160 image-PSF pairs with different RMS in 100 iterations.

4-4 Stop Criterion

With the increase of the number of iteration, although the PSNR of the estimated PSF still shows a increase trend (Figure 4-4), the resolution of the restored image is not always improved, and sometimes, the resolution of the restored image even become worse (Figure 4-5). Therefore, a stop criterion is need to reduce the execution time and avoid the algorithm stopping at the iteration where the estimate may cause the outlier. In this work, the feature of the resolution of the restored image is used to stop the algorithm.

From the resolution measurement in Figure 4-5, it is evident that the resolution of the restored image will fluctuate around a fixed value after several iterations. Therefore, we want to see, if the resolution of the restored image can be used to stop the iteration of the TIP algorithm, and found out that the first derivative of the resolution curve is a good feature to stop the iteration, since it shows the relationship between the change rate of the resolution and the number of the iterations. Commonly, the algorithm is supposed to stop at the iteration where the image reaching the maximum resolution, i.e., the derivative $\nabla Resolution$ at that iteration is zero. However, this threshold is not suitable in this work. Whether PSF will converge to a constant result is not known, since the TIP algorithm is empirical convergence and whether the TIP algorithm is convergent has not been proven mathematically [3]. But it is obvious that reaching the best PSF estimate will take a long time (See Figure 4-4), and only a little improvement is made in the resolution (See Figure 4-5). As a result, another threshold is needed.

In order to find a proper threshold, three possible threshold were tested. The three possible threshold were $-2 \leq \nabla Resolution$, $-1 \leq \nabla Resolution$ and $-0.2 \leq \nabla Resolution$. The performance of these three threshold are shown in Figure 4-7, Figure 4-8 and Figure 4-9 respectively. Compared with the first two threshold which stop the TIP algorithm when most of the resolution improvement are made, the third threshold -0.2 stops the algorithm

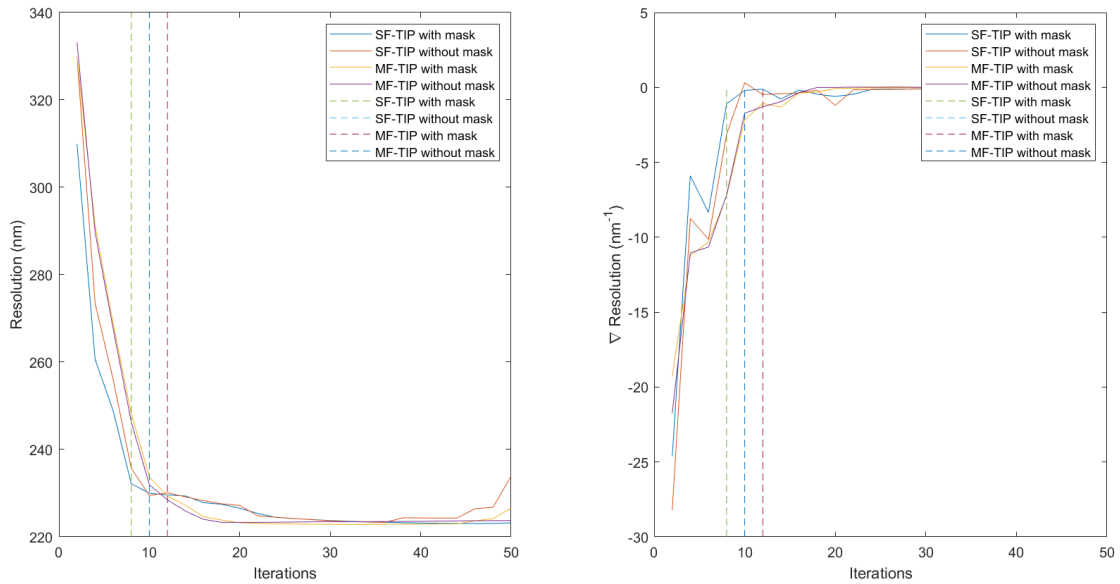


Figure 4-7: The deconvolution result of the SIM data for four TIP frameworks and the first derivative $\nabla \text{Resolution}$ of these deconvolution result respectively. The dash line shows the corresponding iteration for each TIP framework when -2 is used as threshold.

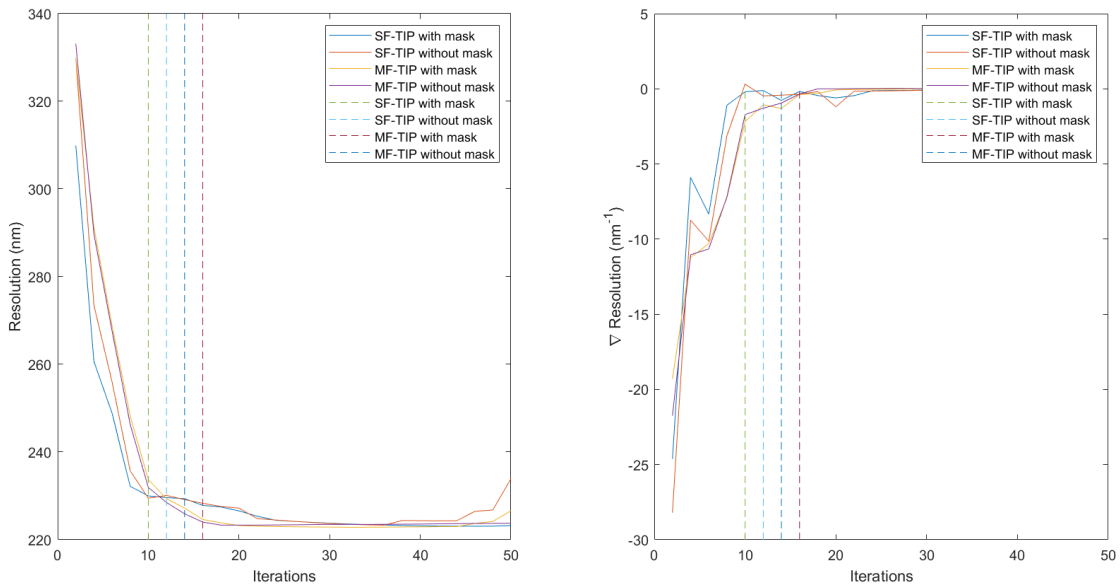


Figure 4-8: The deconvolution result of the SIM data for four TIP frameworks and the first derivative $\nabla \text{Resolution}$ of these deconvolution result respectively. The dash line shows the corresponding iteration for each TIP framework when -1 is used as threshold.

when the resolution of the restored image is nearly complete convergence. Thus, -0.2 is chosen as the threshold for the first derivative of the resolution. Beside -0.2, the 0 is also used as

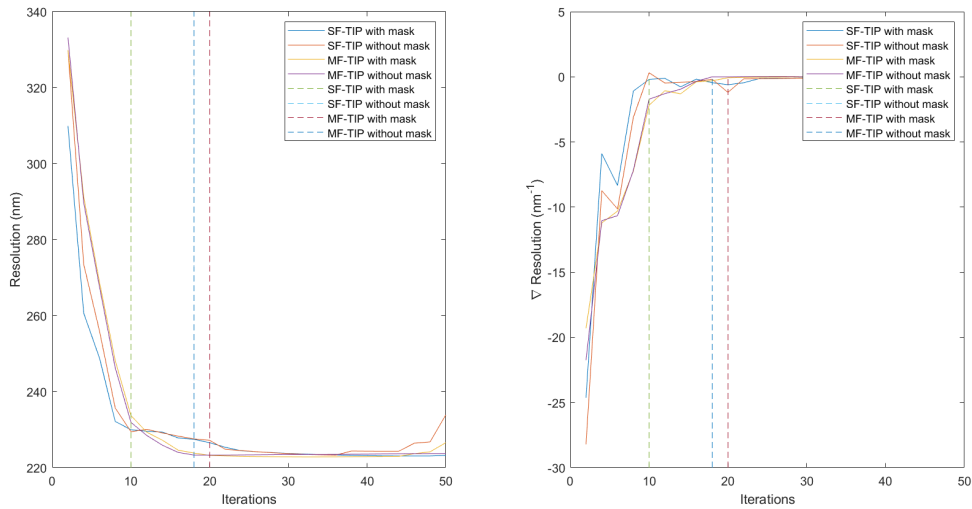


Figure 4-9: The deconvolution result of the SIM data for four TIP frameworks and the first derivative $\nabla Resolution$ of these deconvolution result respectively. The dash line shows the corresponding iteration for each TIP framework when -0.2 is used as threshold.

a threshold, to make sure that the resolution curve shows a decrease trend. Therefore, the threshold used in this work is $-0.2 \leq \nabla Resolution \leq 0$.

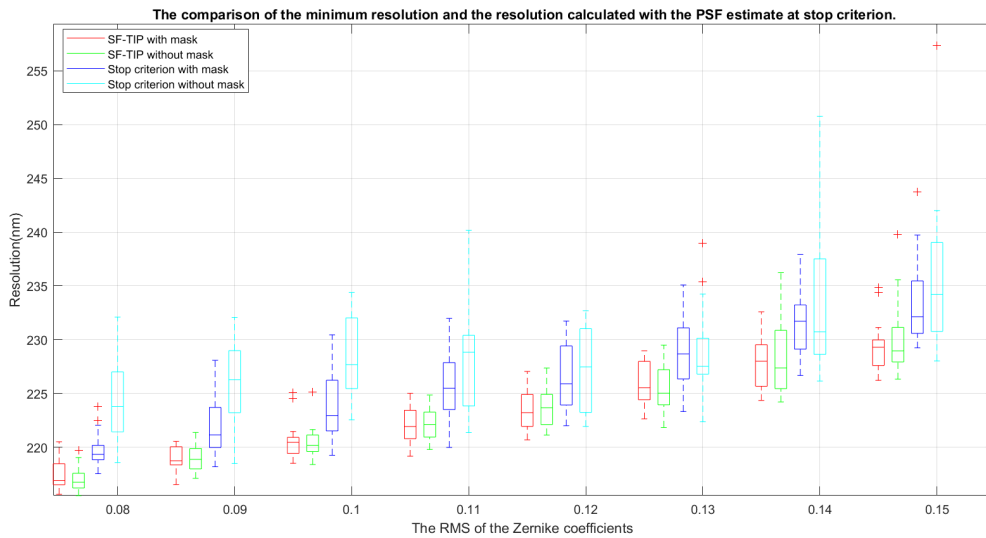


Figure 4-10: The comparison of the distribution of the minimum resolution of the SF-TIP and the resolution of the image restored with the PSF estimate at the stop criterion.

According to Figure 4-10 and Figure 4-11 as well as the Table 4-1, the SF-TIP algorithm with the binary mask for the OTF shows a better performance when the threshold $-0.2 \leq \nabla Resolution \leq 0$ are used to stop the algorithm. The performance of SF-TIP algorithm with the implement of the binary mask here is more stable and more accuracy compared with other

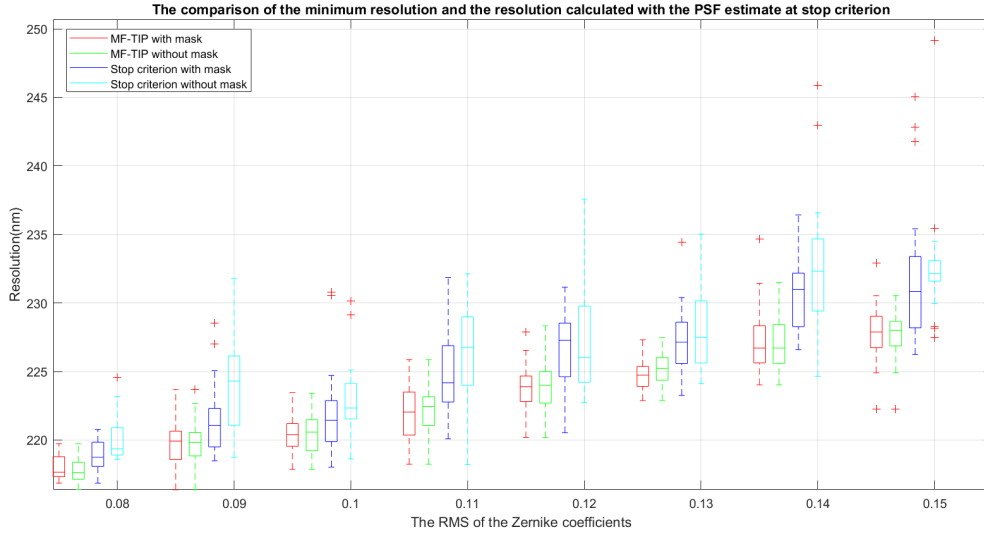


Figure 4-11: The comparison of the distribution of the minimum resolution of the MF-TIP and the resolution of the image restored with the PSF estimate at the stop criterion.

		error (nm)	error < 5	$5 \leq \text{error} < 10$	$10 \leq \text{error}$
Probability	SF-TIP with mask		77.5 %	21.25 %	1.25 %
	SF-TIP without mask		45%	29.375%	25.625%
	MF-TIP with mask		80.625%	13.75 %	5.625%
	MF-TIP without mask		66.25%	25%	10%

Table 4-1: The probability of the error between the minimum resolution and the resolution of the image restored with the PSF estimated at the stop criterion.

algorithms. Thus, the SF-TIP with the binary mask is more suitable for the PSF estimation in SIM.

4-5 Summary

In this chapter, how to implement the TIP algorithm in the SIM is discussed. Compared with the basic TIP algorithm, some modifications are made. A new constraint for OTF created based on the diffraction limit is introduced in the TIP loop. Besides, a threshold for the first derivative of the resolution of the restored image is used here as the stop criterion, which avoids unnecessary iterations.

Chapter 5

Result

This chapter shows the result of SIM simulation and the PSF retrieval with simulated SIM image using TIP algorithm which is introduced in Chapter 4.

5-1 SIM image generation

The experimental parameters used to simulate the optical system were: numerical aperture $NA = 1.4$, refractive index of medium $refmed = 1.47$, refractive index of cover slip $refcov = 1.512$, refractive index of immersion medium $refimm = 1.512$, emission wavelength $ewavelengths = 610$ nm, excitation wavelength $wavelengthex = 565$ nm. The pixel size of the final SIM images is 78nm. No camera offset and gain are considered.

The illumination patterns are generated with three different orientations (-134.3° , -74.8° , 165.5°) and the ideal pattern phases are (0° , 120° , 240°). By using the different number of photons illuminated on the sample, using the Poisson noise, several images with different signal-to-noise (SNR) ratio are generated. Here 7 SIM images are generated with the number of photons $1e8 \sim 1e14$. For each pixel in the image, a 20 photons background noise is added.

The object used in the simulation is Siemens star which is shown in Figure 5-1 and the example of the illumination patterns in three orientations are shown in Figure 5-2.

The Zernike polynomials are used to describe the aberration in the PSF. The strength of the aberration is described by the root mean square (RMS) of the aberration coefficients. To measure the impact of the aberration strength on the performance of the TIP algorithm, the images for 80 PSFs with different RMS of aberration coefficient are generated. The example of the PSF and corresponding OTF are shown in Figure 5-3

The example of the raw images in three orientations generated by the illumination patterns shown in Figure 5-2 are demonstrated in Figure 5-4. To make the image more close to the image of an optical system, the Poisson noise is added. The comparison of the widefield image and the input object are shown in Figure 5-5.

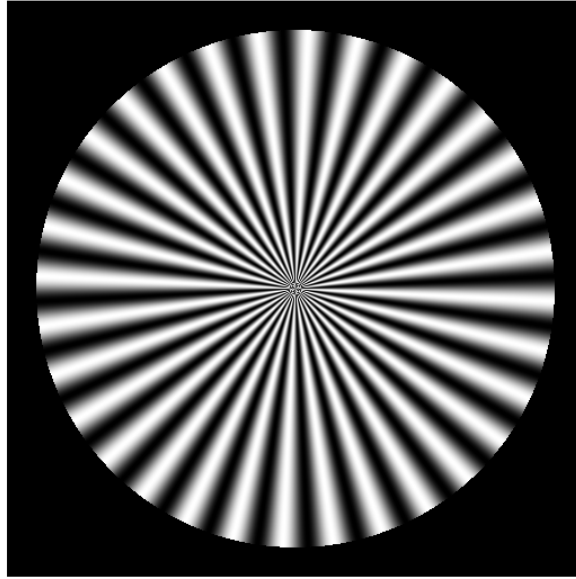


Figure 5-1: The object used in simulation

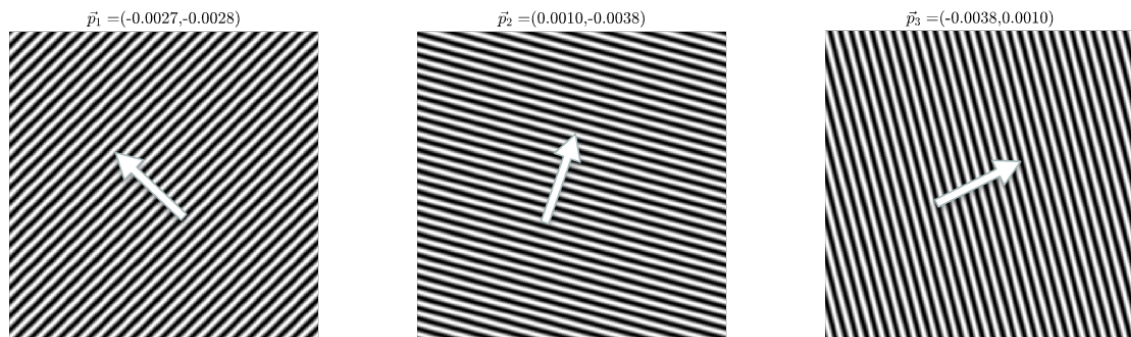


Figure 5-2: The illuminations in three orientations

5-2 The impact of SNR on PSF estimation

Most of the blind image deconvolution algorithm have requirement about the SNR of the image. The low SNR can cause the failure of the PSF estimation and object retrieval. To avoid the error caused by the low SNR, the influence of the SNR on the PSF estimation is analyzed. In order to show the relation between the PSF estimation and the SNR of the image. The PSNR of the PSF obtained from the image with different SNRs are generated, and the resolution of the corresponding restored image are measured. The SNR of an image

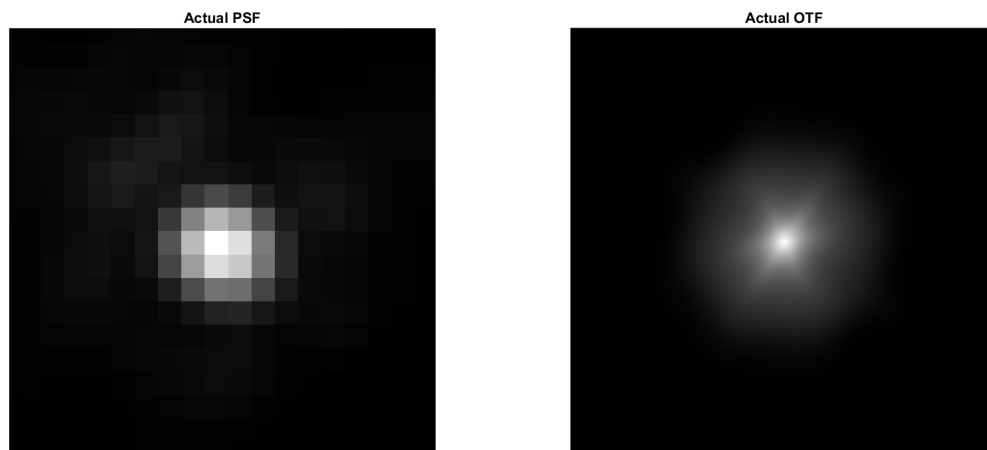


Figure 5-3: The example of the PSF and its corresponding OTF

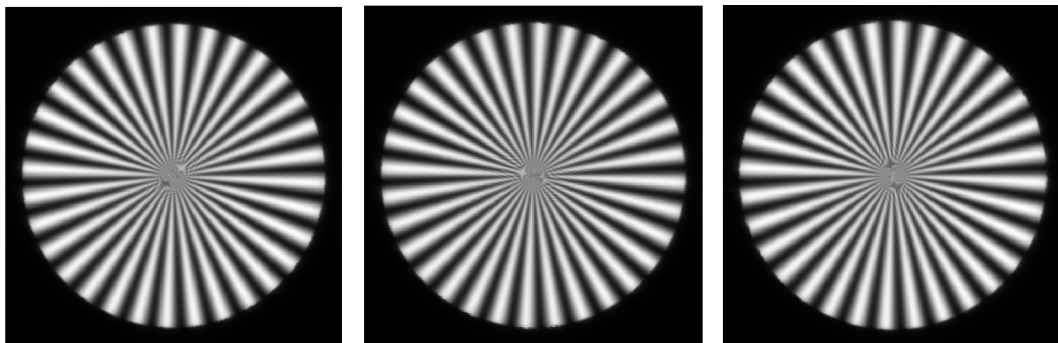


Figure 5-4: The example of simulated raw images in three orientations

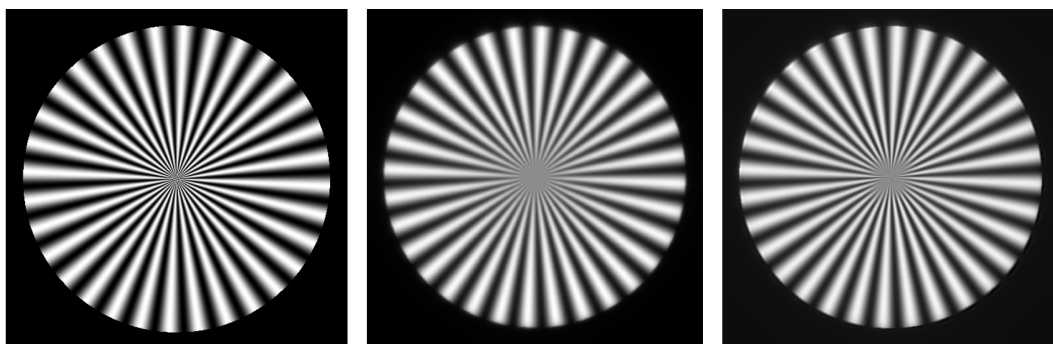


Figure 5-5: From left to right are the object, the wide-field image and the reconstructed image.

is defined in the following manner:

$$SNR = 10 \log_{10} \sqrt{\frac{N_{ph}}{N * N_{bg}}} \quad (5-1)$$

where N_{ph} is the number of the photons for the whole object, N_{bg} refers to the number of the background photon for each pixel, and N is the number of pixel in an image.

The PSNR curves for the PSF obtained from the wide-field images with different SNRs are shown in Figure 5-6. Based on the PSNR curve and the resolution of the image with the retrieved PSF, the TIP algorithm works well in the low SNR case. Although it works well with the low SNR image, a sufficient contrast is still required between the photon per pixel and background noise per pixel. If they have the same order of magnitude, the algorithm didn't work, since the background noise will be considered as part of the object, and the code will crash.

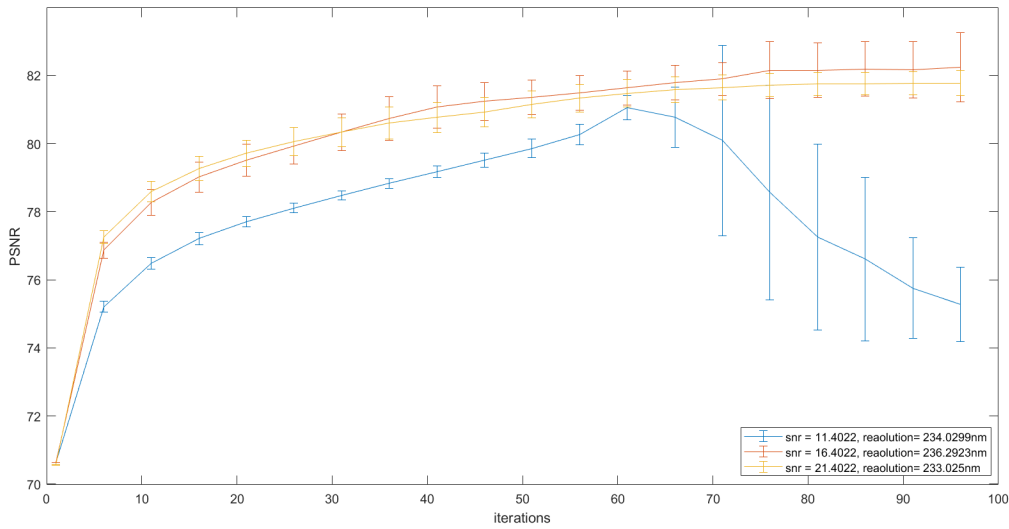


Figure 5-6: The PSNR curve for the PSF retrieve from the widefield image with different SNR using SF-TIP.

5-3 The impact of the aberration strength of the PSF on the PSF estimation

According to Chapter 4, SF-TIP is more applicable than the MF-TIP, in this section the PSF is obtained by the SF-TIP algorithm. The convergence of the TIP algorithm itself is not proved, but the convergence of the performance of the image restoration is shown. With the increase of the quality of the restored PSF, the resolution of the image restored with the PSF won't keep increase. In other to avoid the unnecessary iterations and reduce the execution time, after analyzing the feature of the obtained data, a stop criterion that $-0.2 \leq \nabla Resolution \leq 0$ is introduced.

According to the principle of the SIM image reconstruction introduced in Chapter 2 and the simulation of the SIM image reconstruction described in Appendix A, the PSF-based SIM image reconstruction process can be split into two steps: the parameter estimation and the image recombination. The shift phase (see to Eq. 2-16 and Eq. 2-17) is the main parameter related to the image reconstruction. Before analyzing the quality of restored image, the performance of the phase estimation is measured by calculating the mean and the std of 160 PSF-image pairs, which is shown in the Figure 5-7. With the increase of the amplitude of the

aberration, the error of the phase estimation becomes larger. At the low aberration strength case, the error of the phase estimated with the TIP PSF is close to the phase estimated with the actual PSF, the difference between the phase estimated with these two PSF are similar. However, with the increase of the aberration strength, the difference between these two phase estimation error increases.

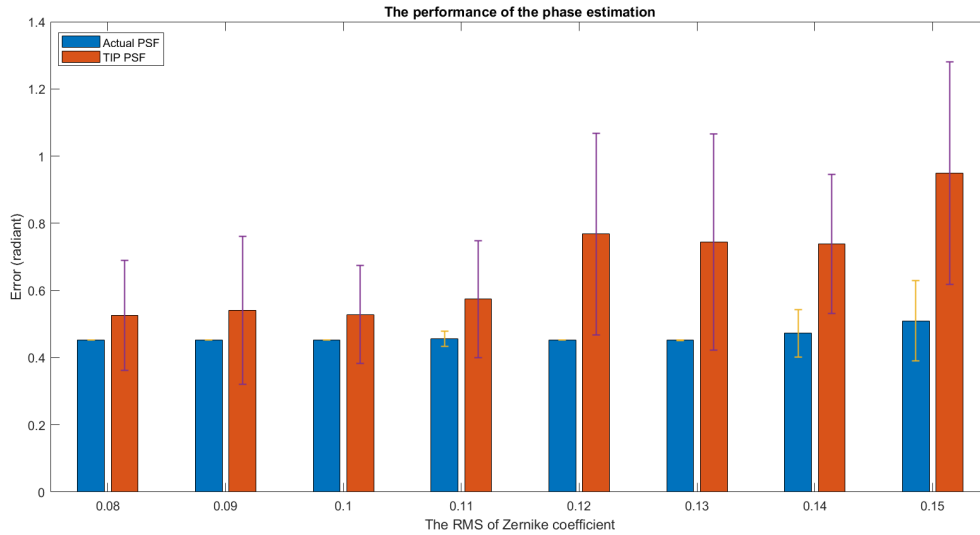


Figure 5-7: The mean and standard deviation of the error of phases estimation. With the increase of the aberration strength, both the mean and the std of the phase estimation error increase.

The phases estimated in the parameter estimation step are then used to shift the information components of the SIM image back to their original position. By recombining all the information components in the Fourier domain, the image reconstruction is achieved. Figure 5-8 illustrate the distribution of the resolution of the wide-field images and restored images with different aberration strength respectively. In Figure 5-8, to make the figure readable, the outliers which are higher than 800nm are removed.

With the increase of the aberration strength, the image becomes more and more blurred. Compared with the wide-field images, the resolution of the restored image shows a significant improvement. According to the boxplot in Figure 5-8, the resolution of these images shows an improvement over 300nm. The mean factors of the resolution improvement for the restored images are shown in Figure 5-9. In the high aberration strength condition, the shape of the PSF is complex, sometimes it is difficult to get an accurate enough estimate, as a result, both the performance of the phase estimation and the image deconvolution is not stable.

5-4 Compare the SF-TIP with the Gaussian curve fitting

In previous section, the performance of TIP algorithm are discussed. In this section, the performance of the TIP algorithm will be compared with the performance of another PSF retrieval method, Gaussian curve fitting method. To measure the PSF of the SIM, the images with several individual beads are generated. The position of these beads are recorded and a

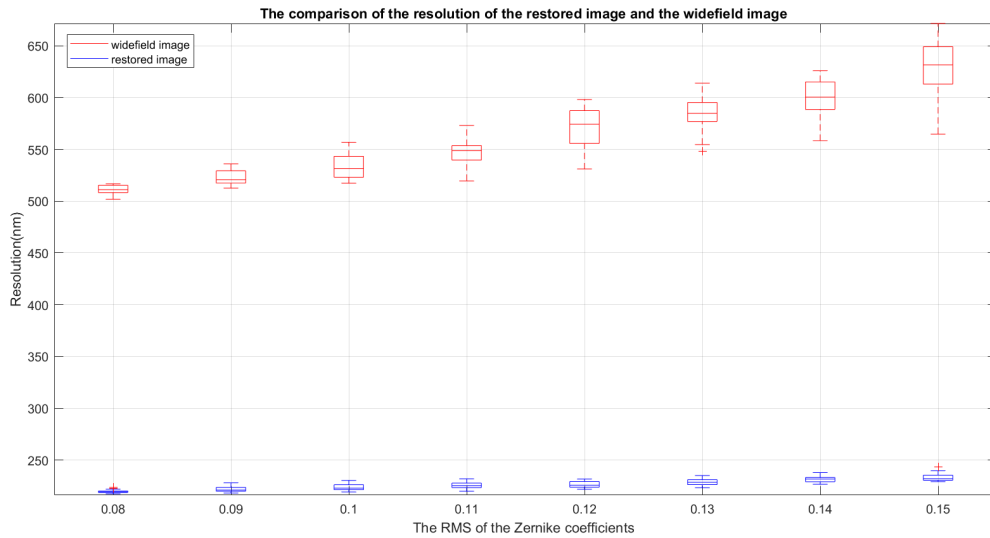


Figure 5-8: The distribution of the resolution of the wide-field images and their corresponding restored images. The resolution of the restored image shows a more than 300nm increase. To make the figure more readable, the outliers for the boxplot which is larger than 800nm are removed.

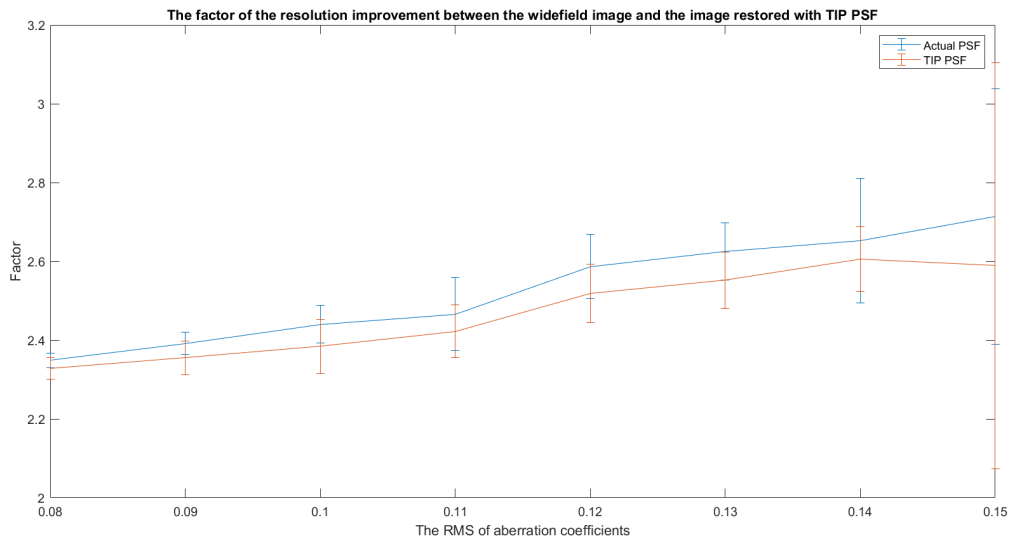


Figure 5-9: The mean factor of the resolution improvement of 160 image-PSF pairs with 8 aberration strength. Errorbar shows the standard derivation of the factor.

small region of interest (ROI) is extracted around each recorded position. Then the image of each beads is centered to the middle of the ROI. By summing all the bead images together, the wide-field image is obtained. Then a Gaussian curve is used to model the PSF[2]. Figure 5-10 shows the comparison of the phase estimation error of the Gaussian fitted PSF, the TIP PSF estimate and the actual PSF.

In the low aberration strength condition, the phase estimation errors of these three kinds of

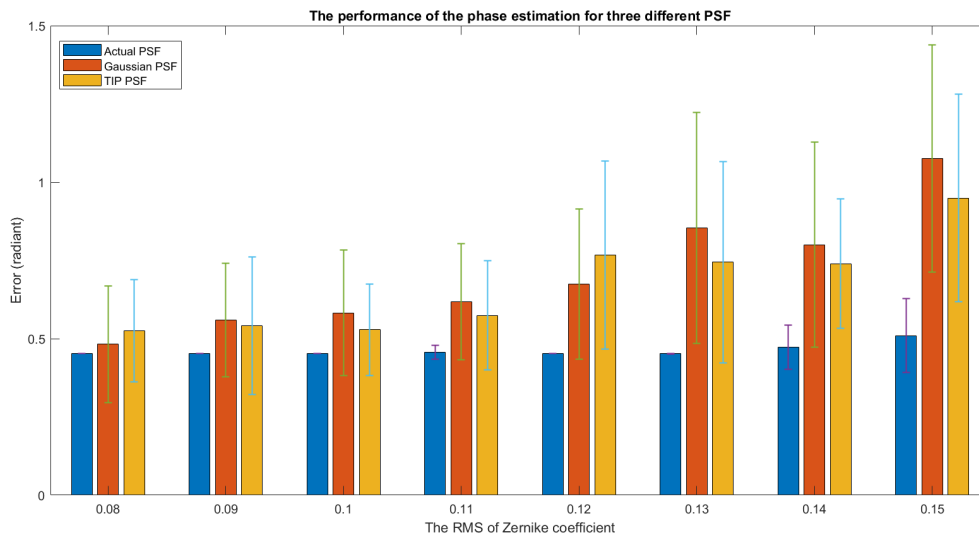


Figure 5-10: The comparison of the mean and standard deviation of the phases estimation error for three different kinds of PSF. In the low aberration strength condition, the performance of these three kinds of PSF are similar. With the increase of the aberration strength, the performance of both the Gaussian PSF and the TIP PSF become worse.

PSF are similar. Both the phase estimated with the TIP PSF and the Gaussian PSF are close to the phase estimated with the actual PSF. With the increase of the RMS of the Zernike coefficients, the shape of the PSF becomes more and more complex, and the Gaussian curve is not good enough to model the aberration in the PSF. For the RMS of the Zernike coefficients larger than 0.12, the performance of the phase estimation with the Gaussian PSF becomes worse than the performance of the phase estimation with the TIP PSF. Besides, both the stability of the phase estimation with the Gaussian PSF and the TIP PSF reduce with the increase of the aberration strength.

The limitation of the Gaussian fitting PSF is also shown in the resolution of the restored image, more precisely, in the image deconvolution. In high aberration case, though both the image restored with the TIP PSF and the image restored with the Gaussian PSF shows the resolution improvement compared with the widefield image, the resolution of the image restored with the TIP algorithm is always better than the resolution of the image restore with Gaussian PSF. The comparison of the resolution of the images restored with these two methods are shown in Figure 5-11. Based on the distribution of the resolution for the image restored with these two kinds of PSF, the TIP algorithm performs better than the Gaussian fitting method. The performance of the image reconstruction with TIP PSF is similar to the performance of the image reconstruction with actual PSF. With the increase of the amplitude of the aberration, the performance of the image reconstruction with Gaussian PSF becomes bad, it is not suitable to be used to do the image reconstruction. The mean factor of the resolution improvement for the image restored with these three kinds of PSF are shown in Figure 5-12. The factor of the resolution improvement for the TIP PSF is close to the factor of the resolution improvement of actual PSF, while the resolution improvement factor for the Gaussian PSF is much smaller than the resolution improvement factor of the TIP PSF, and shows a significant decrease trend with the increase of the aberration strength.

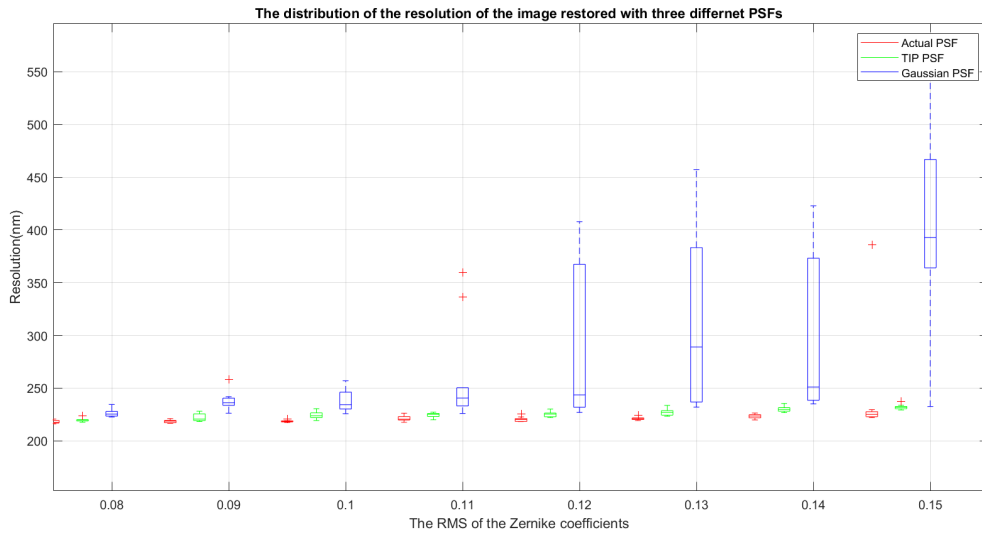


Figure 5-11: The distribution of the resolution of the restored images. The red boxes represent the data for the images restored with the actual PSF, the green boxes are the data for the image restored with the TIP PSF, and the blue boxes are the data for the images restored with the Gaussian PSF. With the increase of the intensity of the aberration, the performance of Gaussian PSF is decreased, and this kind of PSF is not suitable for image reconstruction.

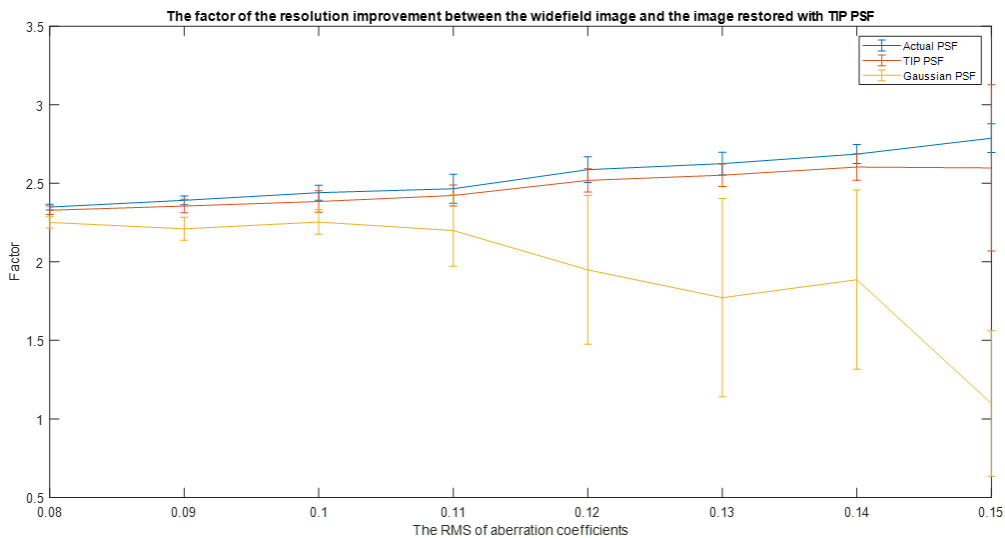


Figure 5-12: The mean factor of the resolution improvement. With the increase of the aberration strength, the stability of the performance of the TIP algorithm decreases. But the mean factor of the TIP PSF is closer to the mean factor for the Actual PSF compared with the factor of the Gaussian PSF

To analysis why the image reconstruction of these three PSFs are different. The example of these three PSFs are visualized. Figure 5-13 shows the actual PSF, the PSF estimated by TIP algorithm and the PSF measured by Gaussian curve respectively. The PSF estimated

by the TIP algorithm is not pixel perfect, but it can retrieve the aberration and the noise in the imaging system, which is better than the Gaussian fitted PSF.

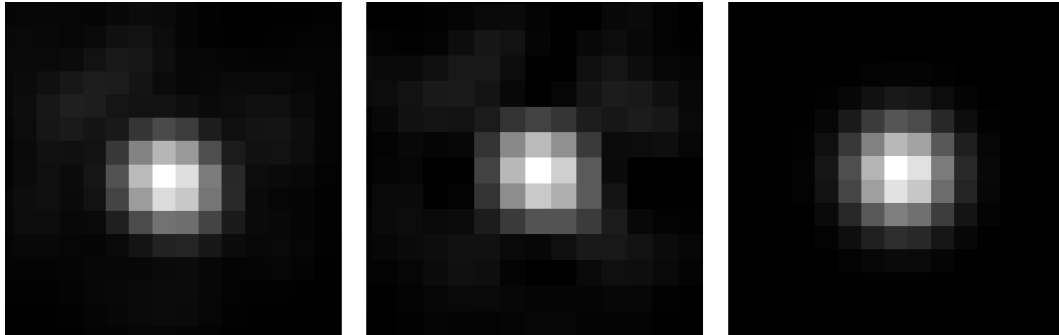


Figure 5-13: The example of the actual PSF and the estimated PSFs. Compared with the Gaussian fitting method, the TIP algorithm performance better in the PSF estimation, since the TIP algorithm is better at retrieving the aberration in the PSF.

In practice, both these two algorithm may calculate wrong PSF. This problem become more intense with the increase of the aberration strength. Since the shape of the PSF is too complex and the size of the PSF is difficult to guess with a high aberration strength. According to Figure 5-10, in the high aberration strength condition, the estimated phase will be far from the actual shift phase. Thus, the information component in the SIM wide-field image will be shift to a incorrect position. Besides, with an incorrect PSF, the image of a point source can not be recovered to a point. As a result, the resolution becomes big. In my experiment, most of the time, the factor of the resolution improvement is larger than 1.5, for the resolution improvement factor which is smaller than 1.5, the image restoration is considered incorrect, in other word, the PSF estimation algorithm fail to obtain the effective PSF. The error of the Gaussian fitting PSF occurs in the high aberration intensity cases, for the low aberration strength case, the Gaussian can be used to obtain an effective PSF. The performance of the TIP algorithm is stable, but it is still possible to obtain an ineffective PSF when the PSF contains too many aberrations. After the RMS of the Zernike polynomials reaches 1.4, the TIP algorithm may obtain an ineffective PSF. The overall success rate of the two PSF estimation methods calculated with these 160 images are shown in Table 5-1. Therefore, compared with the Gaussian fitting method the SF-TIP algorithm is more suitable to be implemented to retrieve an effective PSF from the SIM data.

5-5 Summary

In this chapter, the performance of the image restoration with the PSF estimated by TIP algorithm are talked about. It is obvious that TIP algorithm is a simple, fast way to retrieve the PSF from the SIM image. The performance of PSF estimated by the TIP algorithm are compared with both the performance of the Gaussian fitted PSF and the performance of the actual PSF, the performance of the TIP PSF is close to the actual PSF which is much better than the Gaussian PSF.

	TIP algorithm	Gaussian fitting
RMS = 0.08	100%	100%
RMS = 0.09	100%	100%
RMS = 0.10	100%	100%
RMS = 0.11	100%	100%
RMS = 0.12	100%	90%
RMS = 0.13	100%	70%
RMS = 0.14	95%	65%
RMS = 0.15	85%	25%
All data	97.5%	81.25%

Table 5-1: The success rate of the image reconstruction using the PSF estimated with different algorithms.

Conclusion and Future work

6-1 Conclusion

The aim of this thesis is to estimate the PSF of the structured illumination microscopy with TIP algorithm. This thesis shows the implementation of the TIP algorithm with the SIM images. TIP is an algorithm not only suitable for the multi-frame blind image deconvolution problem but also suitable for the single-frame blind deconvolution problem. And both the framework for the SF-TIP with wide-field image and the framework for the MF-TIP with raw images are introduced in Chapter 4. The performance of PSF estimation with SF-TIP algorithm and MF-TIP algorithm are discussed in Chapter 4. To avoid the over-fitting of the estimated PSF and reduce the execution time of the TIP algorithm a stop criterion are introduced. The result of the PSF estimation with TIP in SIM is illustrated in Chapter 5. And the result shows that TIP is a simple method to retrieve an effective PSF from the SIM data. It is easy to implement and can work with low SNR data.

The implementation of the algorithm requires the user-defined PSF size, to create a support area of the PSF in the spatial domain. This parameter has an impact on the convergence result of the algorithm which need to be defined carefully. Another constraint for the PSF are the support area calculate by the diffraction limit in the Fourier domain, for which all the pixels outside this area in the OTF is assigned 0. This constraint does not help with improving the quality of the PSF estimate, it only helps to find when to stop the iteration. As the intensity of both the PSF spectrum and object spectrum cannot lower than 0, the non-negative constraint is used for these two parameters. The implementation of the SF-TIP with the wide-field SIM image is similar to the framework introduced in [4], except the normalization of the object in the original SF-TIP flowchart is removed, as the split patches are not normalized. Both the MF-TIP and the SF-TIP can help to retrieve the PSF from the SIM data and the performance of them are similar. However, after introducing the stop criterion, the performance of the SF-TIP is better than the performance of the MF-TIP, since the measured resolution of the SF-TIP is closer to the best resolution that can be obtained in the image restoration.

The aberration strength is a factor which has impact on the performance of the algorithm. In optical system, the shape of the PSF is modified by the aberrations. Too many aberration will lead to the shape of the PSF too complex, and it is difficult to reconstruct this kind of PSF with the TIP algorithm. With an inaccuracy PSF, the error of phase shift estimation is large. The information component of SIM image is shifted to wrong position. The use of the inaccuracy PSF also cause problem in image deconvolution. Thus, the TIP algorithm may not work well for the images generated with a too complex PSF. According to Table 5-1, in the high aberration strength cases, the image reconstruction with the TIP PSF may fail.

Hence, if the optical imaging system is well designed, or some aberration removal methods are used in the imaging process of an optical system, in other word, if there are not too many aberrations in the imaging system, TIP algorithm can be used to do the PSF estimation in structured illumination microscopy, and the performance of it is good. If the optical system has too many aberrations, the performance of the TIP algorithm is not stable.

6-2 Future work

The next step for this thesis might find how to define an accurate support region for the PSF. Now, the PSF size is defined based on the user's experience. After testing a set of different PSF sizes, the best one is chosen as the PSF size used to provide the support region of the PSF. The next step might find a method to estimate the PSF size directly based on the SIM data.

Simulation of the Structured Illumination Microscopy

The Simulation of the Structured Illumination Microscopy is done in **MATLAB** (matrix laboratory), an easy-to-use environment and higher performance programming language developed by MathWork, which allows the technical computing, data visualization and user interface creation. Beside, the **DIPlib** and **DIPimage toolbox** are also used. **DIPlib**, a platform independent scientific image processing library written in **C**, is interfaced to **MATLAB** through the **DIPimage toolbox**. The **MATLAB** functions used to create the necessary parameters of the SIM are created by Sjoerd Stallinga.

In this chapter, the simulation of the SIM image formation and SIM object restoration are introduced.

A-1 SIM Image generation

SIM works by using the patterned illumination to illuminate the sample. The pattern used in this thesis is strip. The position and the orientation of the strip patterns are changed a number of times, and the image of the sample is recorded for each one of these changes. The main steps of the SIM system simulation are described below. All the parameters used in the simulation were chosen in such a manner that tried to make the simulation result closest to the actual optical system.

A-1-1 Object preparation

The simulation of the SIM started with the preparation of the object. First a normalized grayscale image is loaded into the workspace which is used as the object. In order to model a fluorescent sample, this object is multiplied by the number of photons. Besides, It is found that the raw SIM images acquired from an optical system contain several background

fluorescence blur. Even though the intensity of the light is weak, it still have impact on the imaging. To make the observed sample as close as possible to the real optical system, for each pixel in this fluorescent sample the background photons was added. The mathematical expression of this process is

$$E = O \cdot Nph + Nbg \quad (\text{A-1})$$

where E denotes the emission distribution of the sample, Nph refers to the number of the photons in the sample and Nbg is the number of the photons in the background. Both the Nph and Nbg are user-defined parameters depending on the situations. Figure A-1 shows the prepared object.

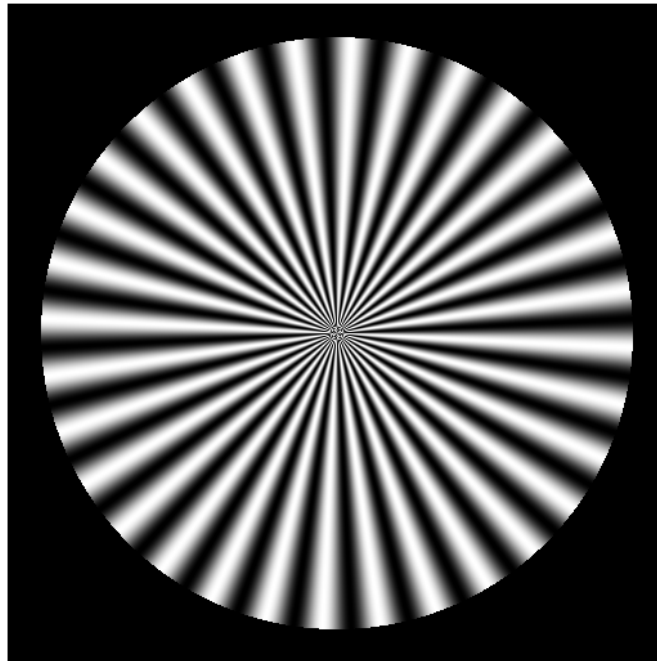


Figure A-1: Prepared object for which $Nph = 1e16$ and $Nbg = 20$. The size of this object is 512×512 .

A-1-2 PSF generation

PSF plays an important role in an imaging system, as it shows the response of this system to a point source. In an aberration free optical system, the intensity distribution of a PSF is Airy pattern. In the case of a real optical system, the PSF is affected by the aberration. In this simulation, the PSF is generated by a set of 12 Zernike polynomials. The Zernike coefficient of these polynomials are generated randomly from -0.05 to 0.05. Before the simulation of the PSF, some parameters of this optical system, like the refractive indices, the NA of the objective lens and the wavelength of the emission light, etc., need to be defined.

The simulation of the PSF is done with 5 main functions. First, the function `get_pupil_matrix` is called to get the pupil matrices, which give the electric field component proportional to its corresponding dipole vector component. The output of this function together with the NA, wavelength (in nm), nominal emitter position as well as the sampling points in both the pupil plane and the image space, are used as the input of the function `get_field_matrix` to calculate the field matrices, which describe the proportion from electric field component to the dipole vector component. Then the fixed dipole PSF can be defined using the function `get_psf`. The example of the PSF is shown in Figure A-2.

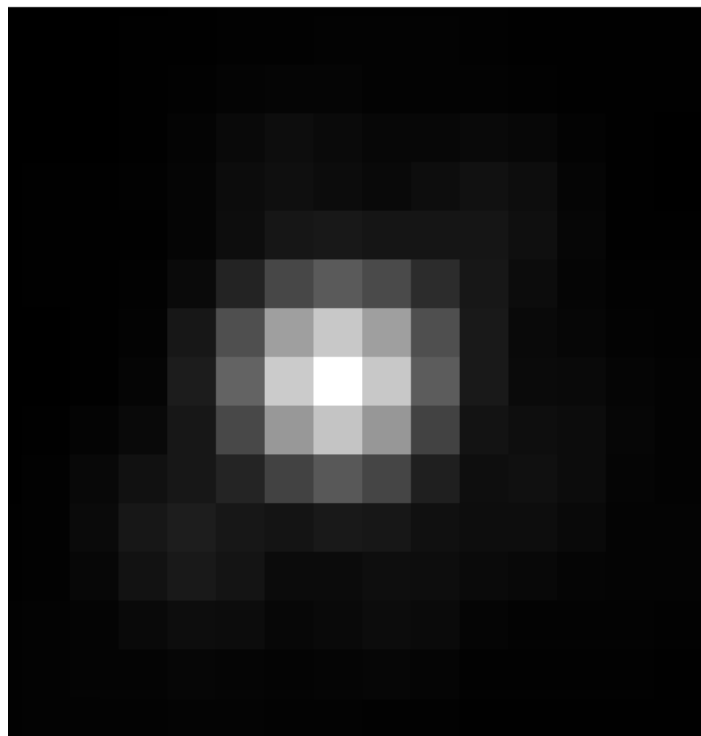


Figure A-2: The simulated PSF

Then the through focus OTF is calculated. In an optical system, the maximum radius of the OTF is limited by the diffraction limit. Therefore a binary mask defined based on the diffraction limit is implemented to remove the out-of-band noise in the OTF. Zero is assigned to all the pixels out of this binary mask. This is done by using the functions `get_otf` and `do_OTFmasking2D`. The example OTF are demonstrated in Figure A-3

A-1-3 Illumination pattern

The illumination pattern used in this simulation is strip. To generate the illumination patterns, the strength of the illumination, the phase and the orientation of the pattern are required. All of them are user-defined parameters which are given at the beginning of the

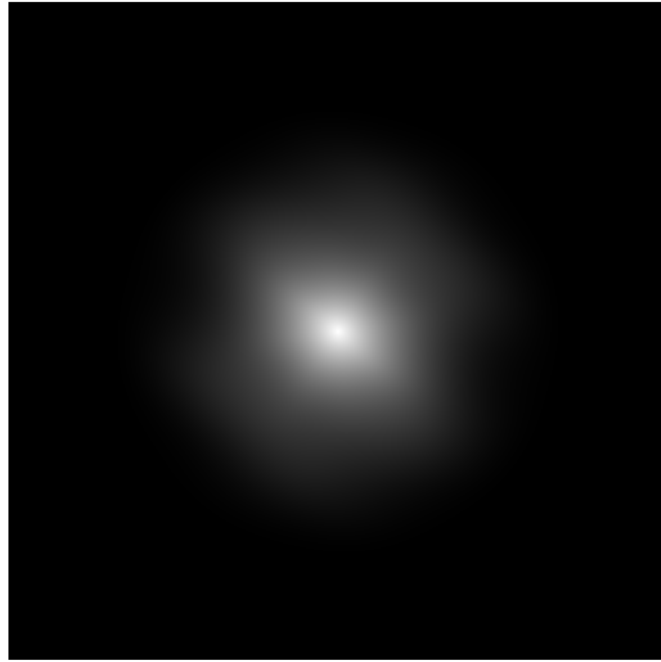


Figure A-3: The example of the OTF of which the out-of-band noise is removed.

code. Eq. 2-11 is the mathematical model of the illumination pattern. The size of the illumination pattern matrix is the same as the object. And then base on this size the coordinates of a rectangular grid is obtained by the function `meshgrid` which is used as the \vec{r} in Eq. 2-11. The vector \vec{p} is calculated by the given orientation. The example of illumination patterns in three orientations are shown in Figure A-4

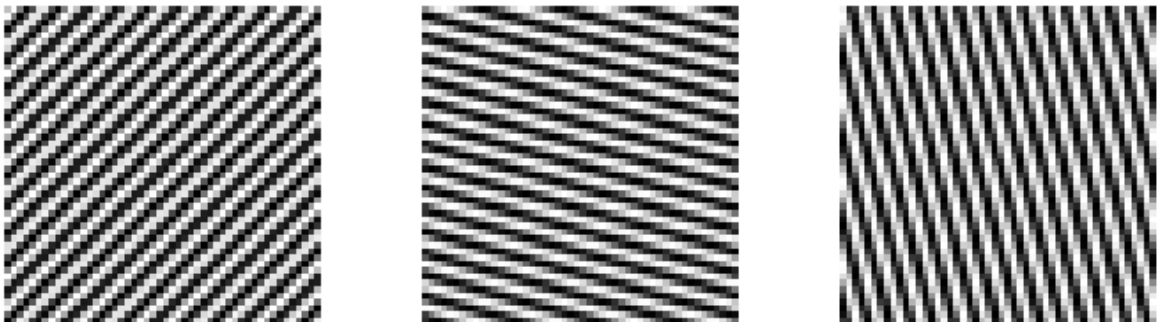


Figure A-4: The illuminations in three orientations

A-1-4 Image Acquisition

In the case of the incoherent imaging, the intensity of the image captured by the sensor is the convolution of the intensity of the emission light from the object and the incoherent PSF. In order to simulate the image formation process, the object is first multiplied by the illumination pattern and then convolved by the PSF. The intensity of the light (or the number of photons) detected by the imaging sensor is fluctuated. The fluctuation of the detected intensity follows the Poisson distribution. Therefore, the formation of each raw image can be written as:

$$raw_{img} = noise((object \cdot pattern) * PSF, 'Poisson') \quad (A-2)$$

Where $*$ is the convolution operator. These steps are done in the function `get_images`. To achieve a 2D-SIM image reconstruction, 9 raw images are required (3 orientations \times 3 phases), while for 3D-SIM image reconstruction, 15 raw images are required (3 orientations \times 5 phases). Figure A-5 is one of the output raw images from the function `get_images`. Then by summing entire raw images together, the wide-field image of this object is obtained (shown in Figure A-6).

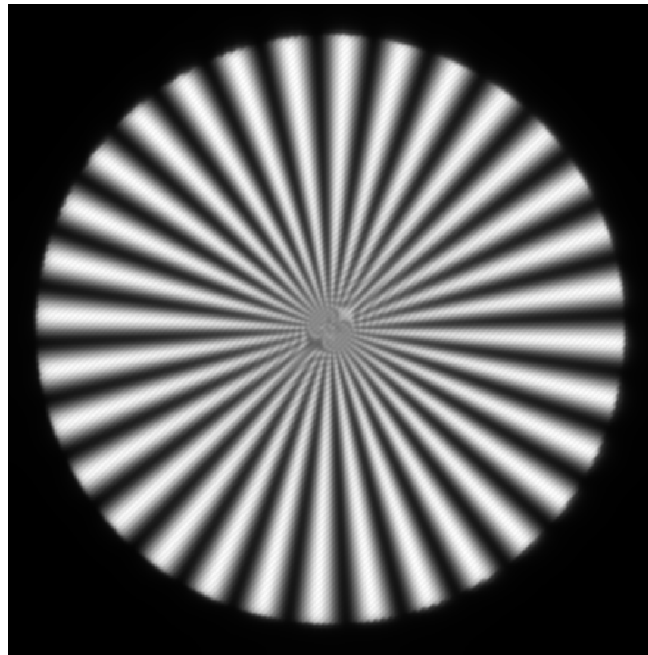


Figure A-5: The example of the SIM raw image.

A-2 Image reconstruction

The process of the image restoration can be split into two main steps: the unknown parameters estimation and the information component recombination with the Wiener filter. The PSF here is a known parameter which is obtained from TIP algorithm.

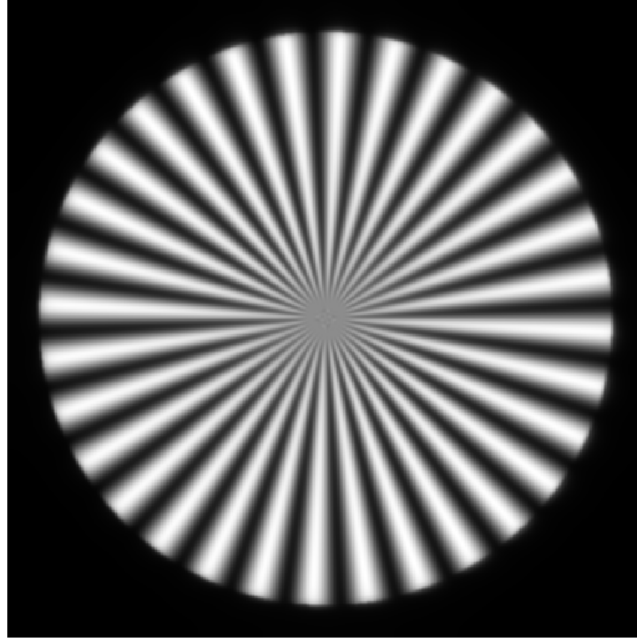


Figure A-6: The wide-field image of the SIM which is the sum of 9 SIM raw images.

A-2-1 Parameters estimation

There are three parameters need to be estimated: the illumination spatial frequency \vec{p} , the initial phase ϕ and the modulation depth a_m .

The determination of the illumination pattern vector \vec{p} and the initial phase ϕ is an iterative optimal process. The iteration starts with finding the peaks of the Fourier Transform of the SIM images. Then using the sub-pixel peak detection method introduced in 2 to increase the precision of the localization of the peaks. For each iteration, the localization of the peak will be modified and a new vector is obtained, when the angle between the current vector and the previous vector reaches the threshold, the iteration will stop. Then by analyzing the auto-correlation of the filtered Fourier images and calculating the phase angle of the complex value (Eq. 2-23), the phase shift estimate is obtained. The estimation of the wave vector \vec{p} and the shift phase ϕ are done in the function `estimate_qvector`.

After getting the illumination spatial frequency \vec{p} and the shift phase ϕ , the laterally shifted copies of the OTF are created. The OTF is shifted to the same location as the location of the information components in the Fourier space. Figure A-7 shows the shifted Fourier components and their corresponding shifted OTFs.

Then the modulation strength can be calculated based on the method introduced in chapter 2. The modulation depth estimation is done by implementing the functions `get_orders2D`, `get_ordershift2D`, and `get_orderstrengths_overlap2D` in turn.

A-2-2 Reconstruction with Wiener filter

The SIM image reconstruction is done by recombining all the information components together in the Fourier domain using a weight-averaging, generalized Wiener filter. The Wiener filter

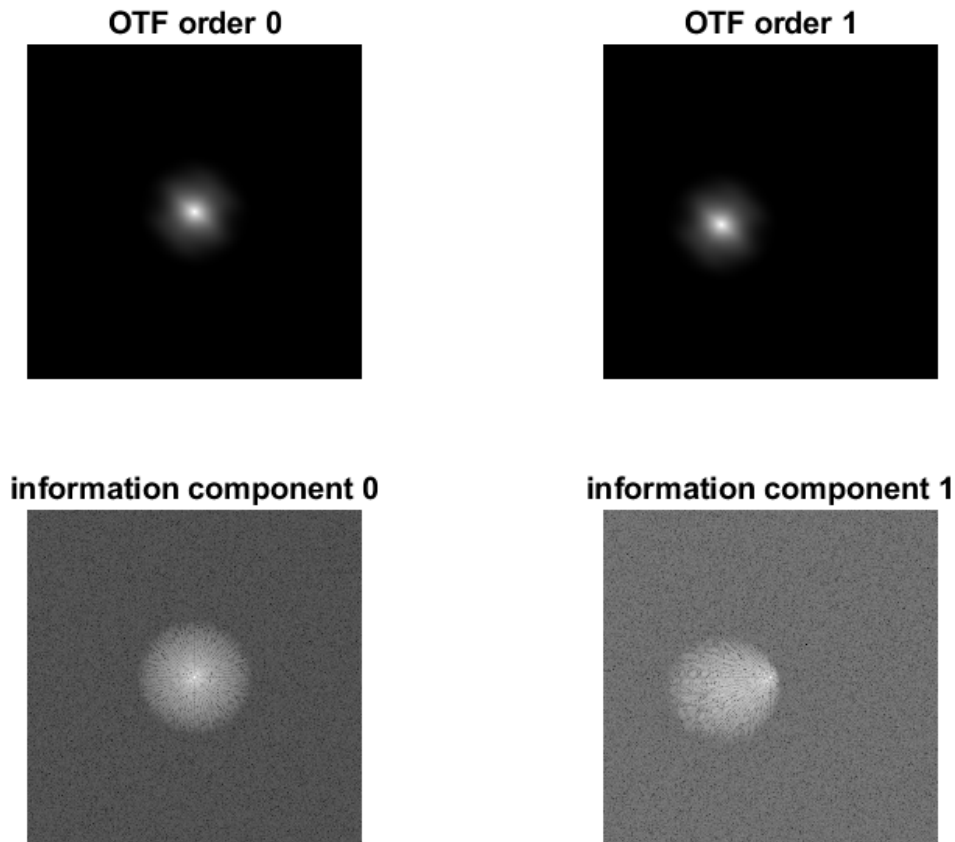


Figure A-7: The shifted Fourier components and the shifted OTF in one orientation.

may introduce ring artifact. The hard edge of the OTF is the main reason of this kind of artifact. To reduce the ring artifact in the reconstructed image apodization filter described in [31], which is introduced in Chapter 2 is applied (shown in Figure A-8). In order to remove the out-of band noise in the OTF, a support region of OTF is defined. This support region is based on the diffraction limit, and zero is assigned to the pixel outside this support region of the SIM-OTF. These two filters are generated in `get_apodization2D`.

Based on the estimated spatial frequency and the shift phase, the information component is unmixed by being shift back to their original location in the Fourier domain. Then the corresponding shifted OTFs, which have the same locations as the shifted information components are calculated. This shifted OTFs are used to generate a filter for its corresponding information component in Fourier domain, and then by summing up all the filtered information components together and implement the Wiener filter, the restored image is obtained. The main functions used here are: `get_reconfuncs2D`, `get_orderfilters2D`, `get_preWiener2DSIMrecon`. The comparison of the wide-field image and the restored image are demonstrated in Figure A-9.

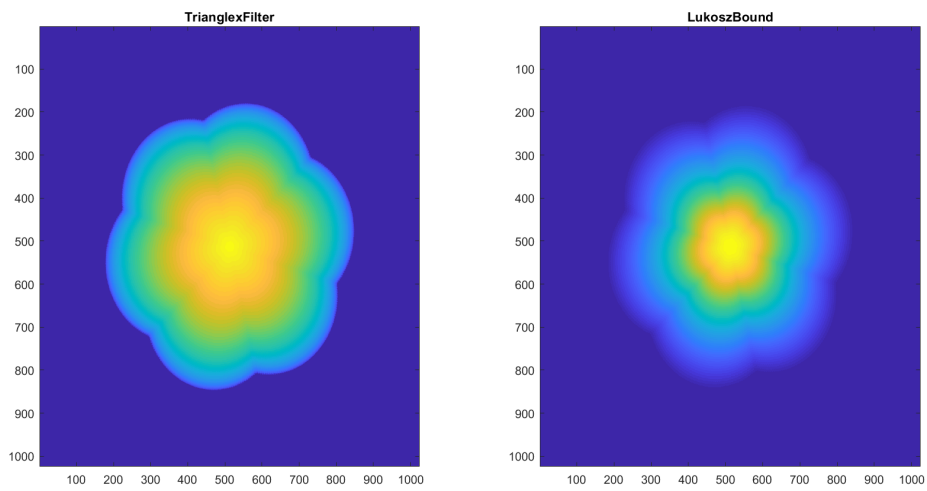


Figure A-8: The possible apodization filters. The LukoszBound is more benign than the trianglex filter for the optimizing the contrast.

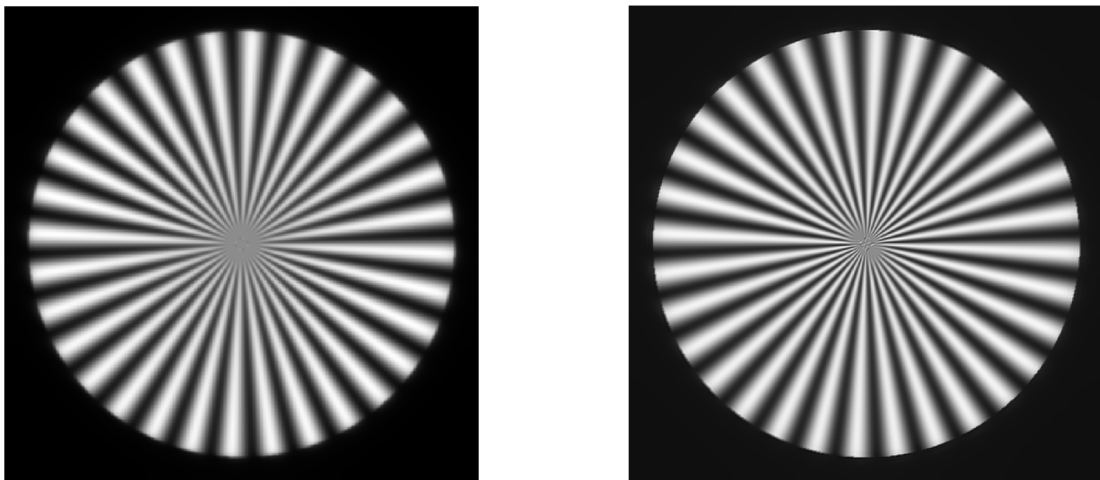


Figure A-9: The comparison of the wide-field image and the restored image. The maximum radius of circle in the wide-field image (left) is larger than the maximum radius of the circle in the restored image (right).

Appendix B

User-defined parameters

The SF-TIP used in this thesis has three real parameters that can be tuned for result. These three parameters are: the number of patches, the circular mask size of the PSF and the size of the Gaussian Apodization mask applied to the patches. The definition and some suggestions about how to define these parameters are described below.

- The number of patches: this parameter determines the number of sub-images in each direction. It depends on the size of the images. Based on my experience, I would like to use the patches which size is 256 px*256 px.
- PSF Size: This parameter is the diameter used to generate a circular mask which is used to create a finite support region of the PSF in spatial domain. The value of it should be restrict in a range where the convergence of the PSF is possible. A diameter that is too small or too big can cause problem in PSF estimation. The diameter of the circular PSF mask should be significantly smaller than the patch size. Another factor need to be considered is the aberration strength, The higher the aberration strength is, the larger the PSF size should be.
- The Gaussian apodization mask: This mask will help to extract the area of the patches used to do the image deconvolution. The size of this area should be between 40%-60% of each patch.

The implementation of the SF-TIP algorithm start with the testing of these three parameters and then get a balance among them. A small Apodization mask will lead to a information loss of the image, which will cause the failure of the PSF estimation. The PSF size need to be tuned carefully to avoid the lose of the convergence of the algorithm.

Measure the resolution of the image

C-1 Measure the quality of the restored image

To measure the quality of the image, the Fourier Ring Correlation (FRC) is introduced [41, 42, 43]. The FRC is a commonly used metric for super resolution image which is applied to the gray-scale images. It measures the normalized cross-correlation between two images in the Fourier domain. The FRC calculation requires two images of the same region with independent noise. In order to get these two images, the binomial random distribution is used to split the super resolution image (shown in Figure C-1) into two sub-images (shown in Figure C-2)

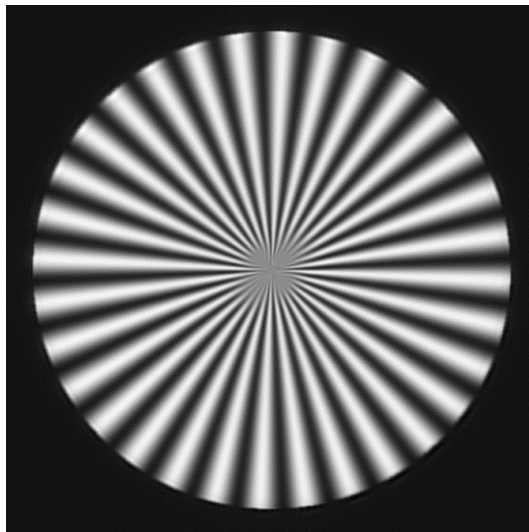


Figure C-1: The restored Siemens star image.

Then a series of concentric rings are created on the spatial spectrum of these two images in Fourier domain. Next the correlation between the pixels located on the rings with same

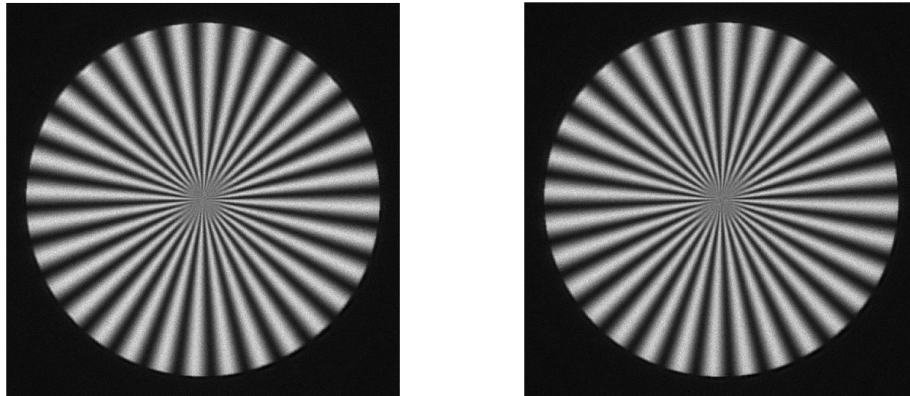


Figure C-2: The two sub-images of the Figure C-1 split using binomial random distribution.

radius in two Fourier transform images are calculated resulting in an FRC curve, which shows the decrease of the correlation with the increase of the spatial frequency.

$$FRC = \frac{\sum_{r \in R} O(r)^* \cdot \tilde{O}(r)}{\sqrt{\sum_{r \in R} |O(r)|^2 \sum_{r \in R} |\tilde{O}(r)|^2}}, \quad (C-1)$$

where $*$ denotes the complex conjugate of O , \tilde{O} is the estimated object in Fourier domain, r is the pixel in the ring R . The resolution of the image is the real space distance of the spatial frequency where the FRC value drops below the $\frac{1}{7}$ (shown in Figure C-3) [41].

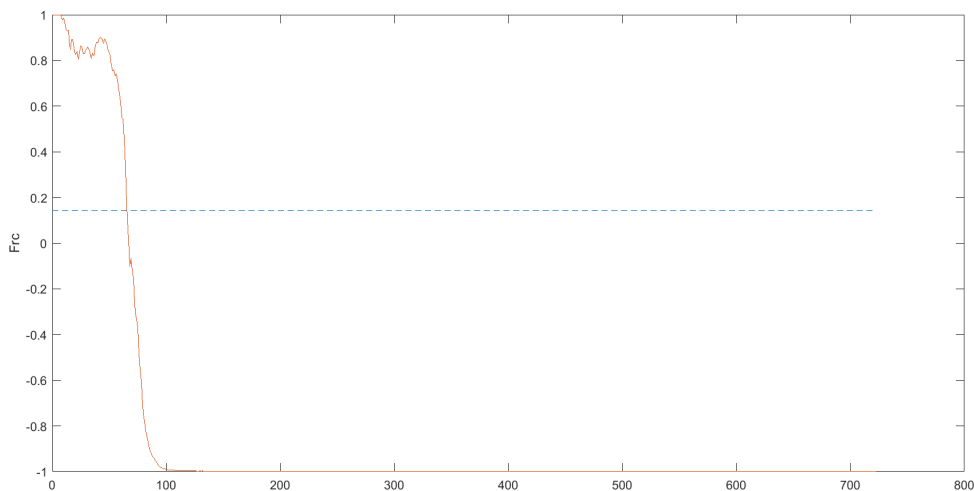


Figure C-3: The example of the FRC curve and the $1/7$ threshold to get the resolution. The real space distance of the x axis value of the cross is the resolution of the image.

Bibliography

- [1] Y. Wu and H. Shroff, “Faster, sharper, and deeper: structured illumination microscopy for biological imaging,” *Nature Methods*, vol. 15, no. 12, pp. 1011–1019, 2018.
- [2] L. M. Hirvonen and T. A. Smith, “Structured illumination microscopy of living cells,” in *2011 International Quantum Electronics Conference (IQEC) and Conference on Lasers and Electro-Optics (CLEO) Pacific Rim incorporating the Australasian Conference on Optics, Lasers and Spectroscopy and the Australian Conference on Optical Fibre Technology*, pp. 766–768, Aug 2011.
- [3] D. Wilding, O. Soloviev, P. Pozzi, G. Vdovin, and M. Verhaegen, “Blind multi-frame deconvolution by tangential iterative projections (tip),” *Opt. Express*, vol. 25, no. 26, pp. 32305–32322, 2017.
- [4] D. Wilding, O. Soloviev, P. Pozzi, C. Smith, G. Vdovin, and M. Verhaegen, “Blind single-frame deconvolution by tangential iterative projections (tip),” *arXiv e-prints*, p. arXiv:1810.07558, Oct 2018.
- [5] M. Verhaegen, P. Pozzi, O. Soloviev, G. Vdovin, and D. Wilding, “Control for high resolution imaging.” Lecture note for the course SC42030, April 2017.
- [6] R. Borlinghaus and L. Microsystems, “Super-resolution on a heuristic point of view about the resolution of a light microscope.” Website, January 2015. <https://www.leica-microsystems.com/science-lab/super-resolution-on-a-heuristic-point-of-view-about-the-resolution-of-a-light-microscope/>
- [7] J. Bewersdorf, R. Schmidt, and S. W. Hell, “Comparison of i5m and 4pi-microscopy.,” *Journal of microscopy*, vol. 222 Pt 2, pp. 105–17, 2006.
- [8] SimphoSOFT, “Simulation of sted microscopy.” Website, 2012. <http://www.simphotek.net/appnote-STED.html>.
- [9] C. Toronto Western Research Institute (TWRI), “Actin fibers.” Website. <https://www.leica-microsystems.com/products/confocal-microscopes/p/leica-tcs-sted-cw/gallery/>.

- [10] J. A. Thorley, J. Pike, and J. Z. Rappoport, "Chapter 14 - super-resolution microscopy: A comparison of commercially available options," in *Fluorescence Microscopy* (A. Cornea and P. M. Conn, eds.), pp. 199 – 212, Boston: Academic Press, 2014.
- [11] E. Betzig, H. F. Hess, H. Shroff, G. H. Patterson, J. Lippincott-Schwartz, and M. W. Davidson, "Education in microscopy and digital imaging." Website. <http://zeiss-campus.magnet.fsu.edu/articles/superresolution/palm/introduction.html>.
- [12] E. H. Rego and L. Shao, *Practical Structured Illumination Microscopy*, pp. 175–192. New York, NY: Springer New York, 2015.
- [13] B. Huang, M. Bates, and X. Zhuang, "Super-resolution fluorescence microscopy," *Annual Review of Biochemistry*, vol. 78, no. 1, pp. 993–1016, 2009. PMID: 19489737.
- [14] M. G. L. Gustafsson, "Surpassing the lateral resolution limit by a factor of two using structured illumination microscopy," *Journal of Microscopy*, vol. 198, no. 2, pp. 82–87, 2000.
- [15] F. Sroubek and P. Milanfar, "Robust multichannel blind deconvolution via fast alternating minimization," *IEEE Transactions on Image Processing*, vol. 21, pp. 1687–1700, 2012.
- [16] R. J. Noll, "Zernike polynomials and atmospheric turbulence*," *J. Opt. Soc. Am.*, vol. 66, pp. 207–211, Mar 1976.
- [17] E. Abbe, "BeitrÄge zur theorie des mikroskops und der mikroskopischen wahrnehmung," *Archiv fÄr mikroskopische Anatomie*, vol. 9, no. 1, pp. 413–418, 1873.
- [18] S. Hell and E. H. Stelzer, "Fundamental improvement of resolution with 4pi-confocal fluorescence microscope using two-photon excitaion," *Opt.Comm*, vol. 93, pp. 277–282, Oct. 1992.
- [19] G. MG, A. DA, and S. JW, "I5m:3d widefield light microscopy with better than 100nm axial resolution," *J. Microsc.*, vol. 195, pp. 10–16, July. 1999.
- [20] M. Schrader and S. Hell, "4pi-confocal images with axial superresolution," *J. Microsc.*, vol. 183, pp. 110–115, August. 1996.
- [21] Y. Garini, B. J. Vermolen, and I. T. Young, "From micro to nano: recent advances in high-resolution microscopy," *Current opinion in biotechnology*, vol. 16 1, pp. 3–12, 2005.
- [22] S. W. Hell and J. Wichmann, "Breaking the diffraction resolution limit by stimulated emission: stimulated-emission-depletion fluorescence microscopy," *Optic Letters*, vol. 19, pp. 780–782, 1994.
- [23] T. A. Klar and S. W. Hell, "Subdiffraction resolution in far-field fluorescence microscopy," *Optic Letters*, vol. 24, pp. 954–956, 1999.
- [24] A. L. McEvoy, D. Greenfield, M. Bates, and J. Liphardt, "Q&a: Single-molecule localization microscopy for biological imaging," *BMC Biology*, vol. 8, p. 106, Aug 2010.

-
- [25] E. Betzig, G. Patterson, O. L. R. Sougrat, S. Olenych, J. Bonifacino, M. Davidson, J. Lippincott-Schwartz, and H. Hess, "Imaging intracellular fluorescent proteins at nanometer resolution," *Science*, vol. 313, pp. 1642–1645, 2006.
- [26] M. Rust, M. Bates, and X. Zhuang, "Sub-diffraction-limit imaging by stochastic optical reconstruction microscopy (storm).," *Nature Method*, vol. 3, 2006.
- [27] K. Wicker, "Non-iterative determination of pattern phase in structured illumination microscopy using auto-correlations in fourier space," *Optics Express*, vol. 21, pp. 24692–24701, 2013.
- [28] S. Shin, D. Kim, K. Kim, and Y. Park, "Super-resolution three-dimensional fluorescence and optical diffraction tomography of live cells using structured illumination generated by a digital micromirror device," *Scientific Reports*, vol. 8, 01 2018.
- [29] M. G. L. Gustafsson, L. Shao, P. Carlton, C.-J. Wang, I. N. Golubovskaya, W. Zacheus Cande, D. A. Agard, and J. W. Sedat, "Three-dimensional resolution doubling in wide-field fluorescence microscopy by structured illumination," *Biophysical journal*, vol. 94, pp. 4957–70, 07 2008.
- [30] A. Lal, C. Shan, and P. Xi, "Structured illumination microscopy image reconstruction algorithm," *IEEE Journal of Selected Topics in Quantum Electronics*, vol. 22, pp. 50–63, July 2016.
- [31] K. Wicker, O. Mandula, G. Best, R. Fiolka, and R. Heintzmann, "Phase optimisation for structured illumination microscopy," *Opt. Express*, vol. 21, pp. 2032–2049, Jan 2013.
- [32] M. Lahrberg, M. Singh, K. Khare, and B. S. Ahluwalia, "Accurate estimation of the illumination pattern's orientation and wavelength in sinusoidal structured illumination microscopy," *Appl. Opt.*, vol. 57, pp. 1019–1025, Feb 2018.
- [33] C. Karras, M. Smedh, R. Förster, H. Deschout, J. Fernandez-Rodriguez, and R. Heintzmann, "Successful optimization of reconstruction parameters in structured illumination microscopy – a practical guide," *bioRxiv*, 2018.
- [34] R. Soummer, L. Pueyo, A. Sivaramakrishnan, and R. J. Vanderbei, "Fast computation of lyot-style coronagraph propagation," *Opt. Express*, vol. 15, pp. 15935–15951, Nov 2007.
- [35] M. Singh and K. Khare, "Accurate efficient carrier estimation for single-shot digital holographic imaging," *Opt. Lett.*, vol. 41, pp. 4871–4874, Nov 2016.
- [36] V. V. Sergei and S. Jefferies, "A new approach to blind deconvolution of astronomical images," *Inverse Problems*, vol. 33, 02 2017.
- [37] G. R. Ayers and J. C. Dainty, "Iterative blind deconvolution method and its applications," *Opt. Lett.*, vol. 13, pp. 547–549, Jul 1988.
- [38] T. J. Schulz, "Multiframe blind deconvolution of astronomical images," *J. Opt. Soc. Am. A*, vol. 10, no. 5, pp. 1064–1073, 1993.
- [39] L. P. Yaroslavsky and H. J. Caulfield, "Deconvolution of multiple images of the same object," *Appl. Opt.*, vol. 33, no. 11, pp. 2157–2162, 1994.

-
- [40] T. C. Wong, T. F. Chan, and C. K. Wong, “Convergence of the alternating minimization algorithm for blind deconvolution,” *Linear Algebra Appl*, vol. 316, pp. 259–285, 2000.
- [41] R. Nieuwenhuizen, K. Lidke, M. Bates, D. Leyton-Puig, D. Grünwald, S. Stallinga, and B. Rieger, “Measuring image resolution in optical nanoscopy,” *Nature methods*, vol. 10, 04 2013.
- [42] N. Banterle, K. H. Bui, E. A. Lemke, and M. Beck, “Fourier ring correlation as a resolution criterion for super-resolution microscopy,” *Journal of Structural Biology*, vol. 183, no. 3, pp. 363 – 367, 2013.
- [43] S. Koho, G. Tortarolo, M. Castello, T. Deguchi, A. Diaspro, and G. Vicidomini, “Fourier ring correlation simplifies image restoration in fluorescence microscopy,” *Nature Communications*, vol. 10, 2019.